Reply to Comments:

Note that original reviewer comments are in bold below, while the author reply is represented by regular type font with bullet points. The tracked changes manuscript is attached after the reply to comments, with removed text in red and added text in blue.

REPLY TO REVIEWER #1

I was surprised to see that other than the Zheng et al. study that looked at the CIRPAS Twin Otter data, no other Twin Otter studies are referenced, so perhaps these data have not been looked at before. I was extremely frustrated by its lack of clarity, rambling unfocused explanations, and grammatical and spelling errors throughout. The number of figures is also disproportionate to the information content of the manuscript.

- We hope that the modifications to the manuscript have addressed your concerns. In particular, we have made most of the recommended changes in regards to your specific comments below, and have hopefully clarified some of the explanations given throughout the manuscript.
- The number of figures remains at 17 (one removed, one added through the revision process). Although yes, this is disproportionate, we also find it reasonable. The nature of this paper remains in characterizing boundary layer turbulence. Characterizing, or to describe something based on its main qualities, involves going over all those qualities in a broad sense. If the paper was focused on a single (or multiple) scientific questions to be answered, the paper would no longer be a characterization. Given the title of the paper, we assume that the reader will be aware of this fact, and understand what it is they are about to read.
- The Twin Otter data is not the primary focus of analysis for other papers that have been published from VOCALS-REx. For example, Jones et al. (2011) and Bretherton et al. (2010), although they analyze the boundary layer structure and decoupling, the data being used is from the NSF C130 and UK BVAe146. Results here can therefore be related to those findings. A discussion has been added to the introduction (see lines 56-68 of the new manuscript) relating previous VOCALS publications to the datasets used.

1) Abstract needs significant tightening and clarification of message. What is the role of radiative cooling? The last two lines could be written much more simply ("lower pressure allows the BL and entrainment zone thickness to increase" plus an explanation in a separate sentence of why turbulence decreases). Mentioning both in one sentence left me scratching my head.

- Hopefully you will find the structure more appropriate. We start the abstract by stating what it is we are going to do, the data we are using, where it was collected, and then provide various results which were found. It should be more focused.
- The role of radiative cooling seems to be out of place in the abstract, but is given more detail (in particular with regards to how radiative cooling is effected by the enhanced

moist layer present on Nov. 1st and 2nd on lines 629-630 and/or 157-159 of the new manuscript.

- The last sentence from the old manuscript has been removed, but a similar statement has been made on lines 7-9 of the new manuscript. Pressure has been used in replacement of geopotential height, and the phrase has been divided into multiple sentences. Note we have replaced geopotential height with pressure when applicable throughout the manuscript.

2) Introduction: Other than the message of "we're going to look at the turbulence data from this field campaign" I didn't get a sense of a focused science question. The authors should rewrite this with the benefits of hindsight to provide that focus.

- We would like to point out, that at no point in the original manuscript did we state "we're going to look at the turbulence data from this field campaign", we do outline our goals in two parts however (please see lines 51-54 in the new manuscript). While yes, these goals are broad, the point of the paper is to look at the in situ data collected to provide a general characterization of the turbulence within the boundary layer. This is a very reasonable objective, as no other paper from VOCALS has analyzed the turbulent data from the Twin-Otter aircraft to this extent. Given that the purpose of the Twin-Otter was to measure turbulent and microphysical properties, a paper which characterizes said turbulence seems more than reasonable (we also find it odd that one has not been published up to this point). We outline this in lines 65-68 of the new manuscript.
- The Twin Otter data is not the primary focus of analysis for other papers that have been published from VOCALS-REx. For example, Jones et al. (2011) and Bretherton et al. (2010), although they analyze the boundary layer structure and decoupling, the data being used is from the NSF C130 and UK BVAe146. Results here can therefore be related to those findings.

3) Section 1.1, there is a general lack of clarity and synthesis. Please be specific about mixing ratio (of water vapor!) and give it a symbol at the outset so its intuitive. Why is the Sc to Cu transition relevant here? "Buoyancy flux is the primary generator of TKE in the STBL" but what drives buoyancy flux? The reader has to read through to pick out the pieces and figure it out. The description of the Bowen ratio is straightforward and the text should be streamlined. Lines 104 through the end of this section ramble. On the other hand, you might explain why a larger latent het flux causes decoupling. Please simplify where necessary and expand where necessary to focus your key questions.

- The mixing ratio has been given a symbol in Section 2.1, where after that point it becomes much more common throughout the text. See line 161-162 of the new manuscript. The latent heat flux and sensible heat flux have also been simplified by using LHF and SHF, respectively.

- The original sentence on the Sc to Cu transition has been removed. Although not relevant, we were simply just pointing out that the process of entrainment and boundary layer deepening plays a key role in the Sc to Cu transition.
- Lines 100-101 in the new manuscript provides a very brief statement on what drives the buoyancy flux. Given that buoyancy arises from differences in density, which depends on temperature and moisture content, having to explain what the buoyancy flux depends on seems rudimentary. The statement in the original manuscript (and in the new manuscript) of "According to Shaw (2003), one of the main sources of TKE in clouds is evaporative cooling and condensational heating, implying the buoyancy flux is the primary generator of TKE in the STBL" on lines 107-110 of the new manuscript and lines 85-88 of the original manuscript also provides the fact that the buoyancy flux is dependent on evaporative cooling and condensational heating.
- The explanation of the Bowen ratio has been simplified. Please see lines 118-119 of the new manuscript.
- The original statements from lines 104 through the end of the section have mostly been removed, even though they describe why the latent heat flux caused decoupling (perhaps you misread this portion). The discussion has been presented in a different format to hopefully make it more straightforward. Please see lines 120-123 of the new manuscript.

4) Section 2.1: Shortwave absorption doesn't only occur at cloud top. Line 142: Don't you mean "on any given day"?

- You are correct, solar absorption does not occur only at cloud top (although this is where it is primarily confined). We have clarified this statement in lines 157-160 of the new manuscript.
- "on any given day" and "from day to day" mean the same thing. However, we have reworded this to "on any given day" on line 173 of the new manuscript.

Given the focus on velocities, surely the instrumentation should be described rather than completely differed to Zhang et. al.?

- A more detailed explanation of the instrumentation, in particular that of the velocity measurements and moisture measurements, has been provided on lines 162-167 of the new manuscript.

5) Section 2.2: You talk about 300-point averaging windows before discussing the sampling time. This is upside-down. Why is linear regression required to get the mean?

- The sampling time is initially discussed in the previous section (2.1) on line 134 of the original manuscript. However, we have corrected this and mentioned that the data used is 40-Hz before discussing the averaging technique on line 184 in the new manuscript.

- Linear regression is not required to get the mean, but it is one of multiple options. Other options include applying just a single mean value, or applying low pass filtering. Please see the figure below for examples of the three methods, all which are based on 320-pt. averaging.

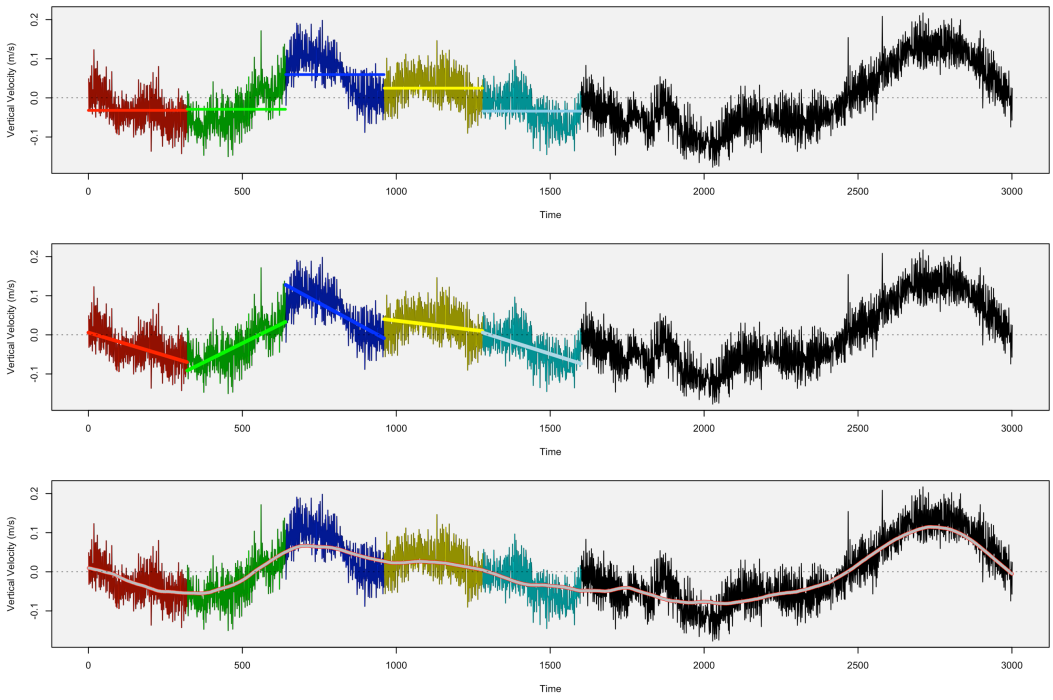

6) "Thetav is commonly used as a proxy for density". Please give a concise theoretical reasoning for this. You mention structure function method but provide no explanation of what it is. Please give a brief one. Simplify line 188. What are "interactions with the plane"?

- Virtual potential temperature is given by: $\theta_v = \theta(1 + 0.61q - q_l)$, where θ is the actual potential temperature and q is the mixng ratio of water vapor, and q_l is the mixing ratio of liquid water in the air. Because water vapor is less dense than dry air, humid air has a warmer θ_v than dry air, while liquid water drops, if falling at terminal velocity, make the air heavier and therefore is associated with colder θ_v. Therefore, θ_v can be used for buoyancy. To be honest, this seems rudimentary to be included in a journal, but has been added nonetheless. Please see lines 200-203 in the new manuscript.
- We are quite confused on "you mention structure function method but provide no explanation of what it is". Please see Equations (5) and (6), which provide the structure function in mathematical form followed by an explanation. Please see lines 113-114 in the new manuscript. We have added a very brief explanation of what a structure function does (i.e., it is just a statistic to analyze common variation in a time series).
- Line 188 in the original manuscript has been simplified. See lines 221-223 in the new manuscript.

- Interations with the plane (at higher frequencies) include aircraft vibrations, etc. Please see Figure 1 Panel (a) in the new manuscript, where the 0.3-5 Hz frequency range is shown as a light gray envelope. 0.3-5Hz covers the inertial subrange of the data, with a spike in energy located at roughly 10Hz, again, attributed to interactions with plane vibrations, etc. This spike in energy is also observed in Jen-La Plante et. al. (2016), where their explanation is "interactions with the plane".

7) Section 3.1: What is omega? Surely it should be defined and given a symbol?

- Omega is the vertical velocity in pressure coordinates (so positive omega is negative vertical velocity), having units of pressure per time. Since much of operational meteorology uses pressure surfaces, omega is a more common quantity to see, especially when quantifying larger temporal scale vertical motions. We have added a brief description of this on lines 275-276 of the new manuscript.

8) Section 3.3: Although you don't have flight data on consecutive days, you do have reanalysis that I expect would be helpful to address boundary layer height changes. (ECMWF?)

- This is a great point, and an excellent addition to the manuscript. Figure 5 in the new manuscript has added ECMWF-BLH data that was derived from the extrapolation of relative humidity (RH) data, where the BLH was determined in the vertical layer that had the largest gradient of RH. There is (relatively) good agreement between the in-situ and ECMWF data, and the ECMWF provides a look at what the BLH did during days where flights did not occur.

Top of page 10: why does enhanced moisture above the BL translate to higher aerosol? Here and elsewhere you would help the reader a great deal by using symbols like z' for normalized altitude, theta, q, etc. – i.e., symbols that are in common use.

- Increased moisture can lead to aerosol swelling for aerosols that are hygroscopic. This means that aerosols that are smaller than the size range being measured by the PCASP (range 0.1 – 2 um) under dry conditions, may increase in size enough under more moist conditions to be measured. This has been discussed on lines 363-365 of the new manuscript. Also, symbols have been added for variables such as z_i (inversion height or BLH), q (mixing ratio) and θ (potential temperature) throughout the new manuscript.

You mention a secondary cloud layer (line 329). Is this a layer of penetrating cumulus? Or something else?

- It is believed to be a layer of cumulus, but not penetrating the Sc deck. The profile of LWC below can give you a better idea of the structure of the profile, where the main Sc

deck is in red, and the secondary cloud layer (cumulus layer) is in blue. See lines 412-414 in the new manuscript.

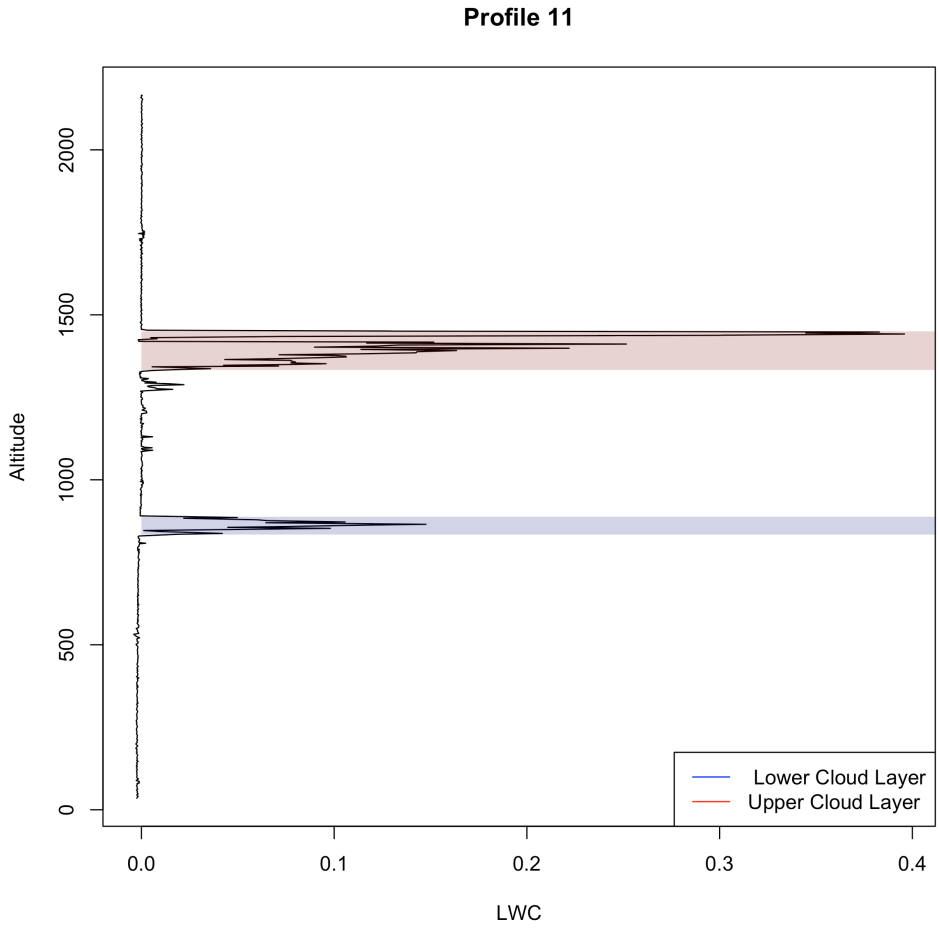

9) Section 4: Line 332, don't you mean horizontal layers?

- We did mean vertical layers, in reference to analyzing the boundary layer through distinct vertical bins or layers (i.e., between z/zi =0 to 0.25, or the bottom ¼ of the boundary layer, etc.). However, we think the paragraph reads better by just removing the sentence in question.

Line 347: This doesn't make sense. An increase in the Bowen ratio means an increase in SHF or decrease in LHF.

- This was a typo, and has been changed to sensible heat flux in the new manuscript (Figure 8 did display the correct information, the text just mixed up the sensible heat flux and latent heat flux). Please see line 438 in the new manuscript.

Line 378: How can Fig. 11 display the same information as Fig 10? Perhaps you mean it has the same format. There are similar instances.

- Yes, we mean that it has the same format as that of Fig. 11. This has been corrected throughout the manuscript. Please see line 468 in the new manuscript for an example.

The use of geopotential height is distracting, and for no good reason. You could make your points much more clearly by talking about pressure. I had to read the text starting from Eq. (9) through to near the end of the section a half dozen times and I still don't know what you are trying to say. Correlations are mentioned and causation is implied. And when it is not, one is left wondering why there is a correlation, and what confounders might be driving the correlation. The summary section might have helped, but it is poorly written, and sometimes repetitive, and circular. Why is geopotential height correlated with sensible heat flux? It may be simple, but at least provide a physical explanation. Stating "agreement with Palm (1996)" doesn't help. The last 3 lines of this section do make sense, and the 'could be' might not be necessary.

- Where applicable, geopotential height has been replaced with pressure. Please see lines 490-495 in the new manuscript for an example (although there are multiple instances where GPH has been replaced with pressure throughout the new manuscript).
- We believe we tried to convey to much information within this section (in regards to discussing the correlations), and as a result it seemed confusing and congested, with no clear start and finish (i.e., circular and repetitive, as you stated). This entire section has been re-written and simplified. Correlations which are not directly discussed in the text have been removed from Table 4. Each paragraph is arranged to discuss a correlation, to go along with a physical explanation for why said correlation exists.
- For example, the second to last paragraph in this section (lines 508-511 in the new manuscript), discuss the correlation between turbulence and pressure and boundary layer height. Correlation values are given, and a physical explanation for this correlation is provided. Again, the last paragraph in this section (lines 512-516 in the new manuscript), discuss the correlation between N_a N_D and drop size with turbulence. Correlation values are given, and a physical explanation for this correlation is provided.
- The summary section has been removed (we feel it is no longer needed with how this section has been re-written), and the last three lines of the section from the original manuscript have been moved to lines 509-510 of the new manuscript, and the 'could be' has been removed.

10) Section 4.2: Line 441, the variance peak at z'=0.99 might simply be because of the strong q gradient. Lines 480-418, you make it sound like the updrafts and downdrafts are meeting in the middle, but they must be spatially displaced.

- You are absolutely correct. The variance due to the strong q gradient is common in most boundary layer vertical profiles of q, and should have been mentioned. This has been added at two points within the new manuscript. Please see line 526 and line 575 in the new manuscript.
- The updrafts and downdrafts are not meeting in the middle. Here, we are simply implying that the peak in w'θ_v' at an in-cloud normalized height of 0.59 (near cloud middle) is due to the w' and θ_v' both being large and positive (i.e., warm moist updrafts, a positive flux)) and due to the w' and θ_v' both being large and negative (i.e., cool dry downdrafts, still a positive flux). This height value of 0.59 just so happens to be where this is a maximum. The flux is still positive throughout the cloud layer however, meaning that warm moist updrafts and/or cool dry downdrafts are present throughout the cloud layer depth, they are just enhanced (or at a maximum) just above cloud middle. If the flux was negative, warm moist downdrafts and/or cool dry updrafts would be dominant.

11) Section 4.3: This entire section should be tightened. I get contradictory messages on the role of precipitation. It can both stabilize the BL (cooling near the surface) or destabilize (cooling higher up). I don't have a clear picture of the precipitation/evaporative cooling profile. Line 558, why bring in the skewness with a single sentence? How does it tie into the text above? What do you mean by "the boundary layer has been turned over"? please be more precise.

- An updated discussion relating to precipitation and its effects on boundary layer stability has been provided. Originally the explanation of precipitation within the boundary layer and how it may change the turbulent profiles was lacking. In particular, lines 635-644 in the new manuscript provide an updated discussion on how precipitation can influence the boundary layer. Feingold et al. 1996 is the original (as far as we know) study to demonstrate how evaporation from precipitation acts to change boundary layer turbulence. If evaporation is occurring in select regions away from the surface (say just below cloud base), the sub-cloud layer will become unstable (i.e., light precipitation is occurring). If evaporation is occurring throughout the vertical sub-cloud layer, and in particular near the surface (i.e., heavy precipitation is occurring), the sub-cloud layer will become stable. The most recent paper that we could find to report findings of this nature is Ghate and Cadeddu (2019), who found that for a similar amount of radiative cooling at the cloud top, the average vertical velocity variance in the sub-cloud layer was about 16% lower during strongly precipitating hours than during weakly precipitating hours. Hopefully the updated discussion provides a clearer picture of what is occurring. Our results (based on profiles of LHF and SHF) demonstrate evaporation occurring away from cloud base, near z/z_i = 0.40 and 0.60 (orange envelopes in Figure 16), leading to the increased turbulent values measured in the sub-cloud.
- We have changed the sentence mentioning the skewness to include the phrase "providing more evidence that" on line 665 of the new manuscript. This is done as to provide more meaning for the skewness in relation to providing further evidence that the boundary layer is decoupled. It is mentioned in previous sections that the skewness is negative for well-mixed boundary layers. We are simply just trying to connect back to

this concept. If needed, we can remove this sentence completely and the reader can just refer to the figure.

- The sentence originally containing the phrase “the boundary layer has been turned over” has been removed from the new manuscript. However, we were simply just referring to the fact that turbulent mixing stabilizes the boundary layer (the mixing reduces the instability, or the boundary layer has been overturned meaning the warm air near the surface and cold air in evaporative regions were mixed together).

12) Conclusions if pressure increased after the passage of the front, why did the BL height increase? The bullets are helpful. The paper would benefit greatly if the conclusions contained more synthesis like this – particularly if focused science questions/hypothesis were addressed. I sincerely hope the authors will focus the revised manuscript around science questions. Lines 610-611: this isn’t an interesting result. It’s an artifact of the sampling. I don’t know why it is in the conclusions. The last lines are so far from the theme of this paper that I wonder why the authors mention these topics.

- A small discussion has been added on lines 699-704 of the new manuscript to address why the BL height increased while pressure (i.e., subsidence) was increasing.
- We have discussed our reasoning in regards to focusing on specific questions/hypothesis in our previous reply towards the beginning of this document. This paper sets out to characterize boundary layer turbulence (there are many papers that simply characterize results from a field campaign, without focusing on specific questions or hypothesis). In regards to the VOCALS dataset, in particular that collected at point Alpha in the twin otter (with an objective to measure turbulence among other things), very little work has been published in regards to the turbulent structure. Most published work revolves around other aircraft and ship based measurements that were made at other sampling regions during VOCALS. For example, Jones et al. (2011) and Bretherton et al. (2010), both which focus on boundary layer structure, decoupling, and precipitation, use data collected from the NSF C-130. Having this characterization of the turbulence in our paper goes a long way toward not only relating to results found in other regions during the campaign, but leads to a better understanding of turbulence on a day to day basis, and what variables can influence it.
- Although not an interesting result, we do believe it is worth mentioning that how one sets out to measure turbulence will ultimately influence the results. Figure 15 is devoted to looking at this through differences when using vertical profiles or horizontal flight legs. Although this is an artifact of the sampling, and the reader can infer that you get vastly different results based on the measurement and averaging methods used, it is still central to the results that are presented and worth mentioning.
- The last three lines pertaining to future work have been removed.

REPLY TO REVIEWER #2

The referencing in this article looks little outdated. Most of the references in the introduction section are from the 80s, 90s, and 00s, and the latest paper is Wood 2012. It will be good if the authors can do a thorough literature review and only refer papers from the last 5-10 years. I completely agree with the authors that the old papers are still valuable and relevant. However, some of the conclusions/speculations reached by the authors have already been made by the subsequent article. It will be good if the authors can improve the referencing. There has been a plethora of stratocumulus-turbulence interaction studies in the last 5-10 years, using the cloud radars and large domain LES models. Line 94-99 document the turbulence structure of stratocumulus topped boundary layers, and it seems that the authors are not aware of recent findings.

- Referencing throughout the article has been updated. Although you make it sound as if we should only refer papers from the last 5-10 years, we have kept most of the original references and added newer (post 2010) references. Previous reviewers of previous articles have been picky about referencing the original papers. However, we do understand the need for having more balance, which we think the current manuscript achieves.
- A total of 42 references have been added (we won't list them out here) throughout the article which are dated 2009 or after, providing a more balanced approach to the references.

In a similar vein, it is unclear to me why the authors have not considered other papers from the VOCALS campaign. Especially as they are all in the VOCALS special issue in ACP. The conclusions similar to this article have been reached by Jones et al., and Bretherton et al. papers in the special issue. It will be a good idea if you can put your results in the context of other studies. Thanks.

- Originally, the lack of other VOCALS papers stemmed from the fact that most of the papers which have been published used datasets other than the Twin Otter at point Alpha. Papers which do use Twin Otter data tend to focus on aerosol and cloud microphysical properties, and not turbulence.
- The Twin Otter data is not the primary focus of analysis for other papers that have been published from VOCALS-REx. For example, Jones et al. (2011) and Bretherton et al. (2010), although they analyze the boundary layer structure and decoupling, the data being used is from the NSF C130 and/or UK BVAe146. However, you are correct in saying that results here can therefore be related to those findings.
- We have added a section to discuss previous VOCALS papers on lines 56-68 of the new manuscript. In particular, results have been related to Jones et al. (2011) and Bretherton et al. (2010), including adding new measures of boundary layer decoupling in Figure 7 that are presented in Jones et al. (2011), as to better relate findings here to their results.
- We also found several instances where we mention findings from Zheng et al. (2011), but fail to circle back around and compare our finding with theirs (A specific example of

this is the statement on lines 407-408 of the new manuscript, and the follow up statement on lines 653-655).

Abstract line 10: the main conclusion of the article is "Findings show that the influence of a synoptic system on Nov 1st and 2nd brings in a moist layer above the boundary layer, leading to a deepening cloud layer and precipitation during passage.". This is contradictory to the notion that moisture above the boundary layer reduces the cloud top cooling, thereby inhibiting turbulence and thinning the clouds. Please see Eastman and Wood (2018 JAS) and other papers.

- The sentence in question here is no longer directly in the abstract. We do discuss the precipitation and synoptic system on lines 13-18 in the new manuscript, and it should be worded more properly. We have also added an extensive discussion on how the moisture above the boundary layer can affect cloud top cooling and other cloud processes. Please see lines 629-634 of the new manuscript.

Do you think that the deepening of the boundary layer might be due to decrease in subsidence or increase in the surface fluxes? In any case, correlation does not imply causation, so maybe you can rephrase this sentence. Thanks.

- The deepening of the boundary layer….do you mean in regards to after the synoptic system passage? In the sentence in question, we state that the cloud layer deepens (becomes more thick). As for the boundary layer height, it remains relatively unchanged between Nov 1st and 2nd (decreases roughly 50-m), but the cloud thickness becomes 100-m thicker. This is due to reduced cloud top cooling limiting the deepening of the boundary layer, while entrainment that is occurring will result in a lower LCL due to the higher moisture content. Please see lines 657-660 of the new manuscript.
- If you were referring to the deepening boundary layer after synoptic system passage, we discuss that on lines 699-704 of the new manuscript.
- It should also be noted, in particular when we are discussing the correlation coefficients, that we do our best to word the phrases properly as to not imply causation. For example, on lines 7-12 in the new manuscript, we state that "As the latent heat flux (LHF) and sensible heat flux (SHF) increases, zi increases, along with the cloud thickness decreasing with increasing LHF." This makes more sense than stating "as zi increases, the LHF and SHF increases." We know that stronger surface fluxes will increase zi, but the correlation coefficients only tell us that they are correlated, not which causes the other. Everything should be phrased properly throughout.

Section 2.2 documents the way turbulence statistics have been calculated. It will be good if you can also include some sort of error analysis in it. I suspect the differences in you see are not statistically significant. This is often the case, however you should at least document these. Your results still should be relevant. The w'N' and the skewness of vertical velocity are

the prime suspects in my opinion. Please see papers by David Turner and Wulfmeyer on the calculation of higher order moments.

- We have added several paragraphs at the end of Section 2.2 (See lines 227-265 in the new manuscript) addressing these concerns. You are correct that they should be documented. Figures 16 and 17 have also had the raw calculations added to the profiles of w'N' and w'w'w', which clearly shows that the mean values that were being displayed are NOT statistically significant (as you assumed).

Also, how good are the temperature and humidity measurements within the cloud layer. The sensors suffer from significant drop shattering and cooling. Can you please discuss if the measurements are sufficient for calculating buoyancy fluxes. Thanks.

- Please see lines 162-167 in the new manuscript, which addresses the concerns laid out above. Although we have a limited capacity to the detail and length of explanation which can be given within the manuscript, we think the information added should address the concerns. Also, if you are curious, you can see the links provided for more information on the total set up of the Twin Otter, which has taken great care to make the most accurate measurements possible.

https://archive.eol.ucar.edu/projects/post/meetings/200902/documents/khelif_POST_SLC_Feb_2008_sm.pdf

https://www.researchgate.net/figure/UCI-Turbulence-instrumentation-on-the-CIRPAS-Twin-Otter-in-POST-and-VOCALS-REx-field_fig1_228968823

You are confusing the inversion layer and the entrainment zone. These are two different things. The entrainment zone is within (plus-minus 25 m) of the cloud top, while the inversion layer can span 100s of meters at a times. There is no known mechanism that can bring air from above the top of the inversion into the cloud layer. This needs to be changed throughout the document. Please see papers by Juan-Pedro Mellado. Thanks.

- You are correct. We (multiple times) exchanged the terms inversion layer and entrainment zone. This has been corrected throughout the manuscript and a more accurate explanation has been added. In particular, see the discussion added in the introduction on lines 89-96:

"The boundary layer top is characterized by several strong gradients, including the cloud boundary (gradient in LWC), the entrainment zone (gradient in vorticity, where the entrainment zone separates regions of weak and strong mixing between laminar flow above and turbulent flow below), and the capping inversion (gradient in potential temperature). The cloud boundary typically lies in the entrainment zone (Albrecht et al. 1985, Malinowski et al. 2013), which in turn lies in the capping inversion, although these layers do not necessarily coincide (Mellado, 2017). Turbulent analysis of these layers in Jen La Plant et al. (2016) found that turbulence (both TKE and TKE dissipation) decreases moving from cloud top into the free atmosphere above, where mixing of the laminar and turbulent flows occurs within the entrainment layer."

- All subsequent discussions of entrainment have been modified within the manuscript. Although there are multiple examples of this throughout the manuscript, please see lines 485-486 within the new manuscript for a specific example. All original explanations which made it sound like air was being entrained from above the inversion layer has been corrected.

One of the main conclusions is that "A maximum in TKE on Nov. 1st (both overall average and largest single value measured) is due to precipitation acting to destabilize the sub-cloud layer, while acting to stabilize the cloud layer.". This contradicts your earlier statement in the introduction about evaporating drizzle stabilizing the sub-cloud layer. There have been LES modeling studies and some observational studies showing drizzle to stabilize the sub-cloud layer, directly contradicting your conclusions.

- An updated discussion relating to precipitation and its effects on boundary layer stability has been provided. Originally the explanation of precipitation within the boundary layer and how it may change the turbulent profiles was lacking. In particular, lines 635-644 in the new manuscript provide an updated discussion on how precipitation can influence the boundary layer. Feingold et al. 1996 is the original (as far as we know) study to demonstrate how evaporation from precipitation acts to change boundary layer turbulence. If evaporation is occurring in select regions away from the surface (say just below cloud base), the sub-cloud layer will become unstable (i.e., light precipitation is occurring). If evaporation is occurring throughout the vertical sub-cloud layer, and in particular near the surface (i.e., heavy precipitation is occurring), the sub-cloud layer will become stable. The most recent paper that we could find to report findings of this nature is Ghate and Cadeddu (2019), who found that for a similar amount of radiative cooling at the cloud top, the average vertical velocity variance in the sub-cloud layer was about 16% lower during strongly precipitating hours than during weakly precipitating hours.
- The earlier statement in the introduction was referring to the explanation provided in Zheng et al. (2011). It is stated that "Zheng et al. (2011) suggest drizzle processes act to stabilize the boundary layer, leading to decoupling on Nov. 1st." I have circled back around to this statement on lines 653-655 of the new manuscript, stating that Zheng et al. is correct in stating that drizzle acts to decouple the boundary layer, but wrong in suggesting that it acts to stabilize the boundary layer as well.

Minor Comments:

Line 236-237: This has been already stated in the introduction section, so please remove. Thanks.

- We have removed the statement in question from the new manuscript.

Line 268: The modulus of a number does not read well. I think you mean the absolute change. Maybe you can just mention (absolute change > 0.1)? Thanks.

- You are correct in that we mean the absolute change. We have taken your advice and made the necessary corrections. Please see lines 341-343 in the new manuscript.

Equation 9 seems out of place. I am not sure if it conveys anything meaningful.

- This equation has been removed, although what the equation conveys has been kept. Please see lines 491-495 in the new manuscript. We were just trying to relate that the boundary layer height changes based on entrainment and large scale subsidence. This can easily be described, as opposed to showing the equation however.

Figure 1: Covert Omega to Pa/day and put latitude and longitude in regular (-ve for southern hemisphere) units.

- The units have been converted to hPa/day, which is much more relatable than the original Pa/second. We are also unsure what you mean by –ve for the latitude units. However, we have changed the latitude and longitude labeling to match what has been published in previous VOCALS-REx publications. (see Zhang et al. 2011, Toniazzo et al. 2011, Rahn and Garreaud 2010). If you would prefer a different unit or way of labeling, we would be more than happy to change it.

Figure 2: Panel (b) is surface air temperature?

- Yes, it is surface air temperature. This has been added to both the figure description and figure label. See Figure 3 in the new manuscript.

Figure 3: Please convert Omega to Pa/day. The figure also doesn't tell much, so maybe you can move it to supplemental material.

- This figure has been removed, especially since we already have a large number of figures presented.

Figure 4: Instead or in addition to the wind roses, it will be good if you also show the profile of wind speed. Thanks.

- We have kept to wind roses, but have also added a vertical profile for wind speed. Please see Figure 4 Panel (e) in the new manuscript.

Turbulent and Boundary Layer Characteristics during VOCALS-REx

Dillon S. Dodson[1] and Jennifer D. Small Griswold[1]

[1]Department of Atmospheric Sciences, University of Hawaii, Manoa, Honolulu, HI, USA

Correspondence: Jennifer D. Small Griswold (smalljen@hawaii.edu)

Abstract.

Stratocumulus clouds have a significant impact on climate due to their large spatial extent, with areas of enhanced coverage termed stratocumulus decks. How turbulence evolves with time and influences the stratocumulus deck properties however, in particular throughout the vertical profile of the boundary layer, is still lacking through model parameterizations of the small-scale flow. Collecting in situ data to better understand the turbulence and physical processes occuring within the stratocumulus deck therefore key to better model parameterizations. Boundary layer and turbulent characteristics (surface fluxes, turbulent kinetic energy (TKE), turbulent kinetic energy dissipation rate (ϵ), etc.), along with synoptic scale changes in these properties over time, are examined using data collected from 14 research flights made with the CIRPAS Twin Otter Aircraft. Data was collected during the VOMOS Ocean-Cloud-Atmosphere-Land Study-Regional Experiment (VOCALS-REx) at Point Alpha (20°S, 72°W) in October and November of 2008 off the cost of South America (20°S, 72°W). The average boundary layer depth is found to be 1170-m, with 28% of the boundary layer profiles analyzed displaying decoupling. Analysis of correlation coefficients indicate that as atmospheric pressure decreases, the boundary layer height (z_i) increases, accompanied by a decrease in turbulence within the boundary layer. As z_i deepens, cooling near cloud top cannot sustain mixing over the entire depth of the boundary layer, resulting in less turbulence. As the latent heat flux (LHF) and sensible heat flux (SHF) increases, z_i increases, along with the cloud thickness decreasing with increasing LFH. This suggests that an enhanced LHF results in enhanced entrainment which acts to thin the cloud layer while deepening the boundary layer.

A maximum in TKE on Nov. 1^{st} (both overall average and largest single value measured) is due to precipitation acting to destabilize the sub-cloud layer (through evaporation away from the surface), while acting to stabilize the cloud layer. Enhanced moisture above cloud top from a passing synoptic system also acts to reduce cloud top cooling, reducing the potential for mixing of the cloud layer. This is observed in both the vertical profiles of the TKE and ϵ values, where it is found that the distributions of turbulence for the sub-cloud and in-cloud layer are completely offset from one another, with the TKE in the sub-cloud layer maximizing for the analysis period, while the TKE in the in-cloud layer is below the average in-cloud value for the analysis period. Findings show that the influence of a synoptic system on Nov 1^{st} and 2^{nd} brings in a moist layer above the boundary layer, leading to a deepening cloud layer and precipitation during passage, and a large increase in boundary layer height and cloud thinning after passage. The maximum value in turbulent kinetic energy (TKE) was measured on Nov. 1^{st} due to precipitation destabilizing the sub-cloud layer while a minimum occurred on Nov. 2^{nd} after precipitation had ceased due to turbulent mixing overturning the boundary layer and depleting the initial turbulent energy produced from the evaporation of

precipitation below cloud base. Turbulent properties Measures of TKE, ϵ, and the buoyancy flux averaged over all 14 flights reach display a maximum near cloud middle (between normalized in-cloud values of 0.25-0.75), with well mixed boundary layers experiencing two peaks in TKE, one near cloud base due to latent heat release and another near cloud top due to evaporational cooling. Seven of the fourteen flights display two peaks in TKE within the cloud layer, one near cloud base and another near cloud top, signifying evaporative and radiational cooling near cloud top and latent heating near cloud base. Overall, it appears that turbulence measured at Point Alpha is weaker than that measured over the open ocean to the west of Point Alpha, and that measured during other scientific campaigns. Synoptic scale analysis suggests that as the geopotential height decreases, the boundary layer height and entrainment zone thickness increases, accompanied by a decrease of in-cloud and below-cloud turbulence, and vice versa.

1 Introduction

Stratocumulus (Sc) clouds have a significant impact on climate due to their large spatial extent, covering approximately 20% of Earth's surface (23% over the ocean and 12% over the land) in the annual mean (Randall et al., 1984). According to Wood (2012), the subtropical eastern oceans in particular are marked by extensive regions of Sc sheets (often referred to as semipermanent subtropical marine stratocumulus sheets). Of those, the largest and most persistent Sc deck in the world, the Peruvian Sc deck, lies off the west coast of South America (Bretherton et al., 2004), making its role in climate an essential building block to better improved modeling by the overall earth system. A better understanding of not only the Peruvian Sc deck, but all Sc decks, is therefore necessary to make advancements in modeling and representing the present-day and future climate system. improve our physical understands of mechanisms controlling Sc clouds, and to improve confidence in climate model sensitivity (Zhang et al., 2013), especially considering climate models suffer from order-one uncertainties in Sc cloud representation (Noda and Satoh, 2014; Gesso et al., 2015).

It is a challenge for models to successfully simulate the Peruvian Sc deck due to the importance of subgride scales and physical processes which are poorly represented (Wood et al., 2011). In particular, mMost models continue to struggle with the boundary layer vertical structure (Wyant et al., 2010) which is important for determining Sc cloud properties. One example, as discussed in Akinlabi et al. (2019), is that a robust estimation of the turbulent kinetic energy dissipation rate (ϵ) is needed when creating subgrid models for Lagrangian trajectory analysis of passive scalars (Poggi and Katul, 2006) or large-eddy simulation. For example, Other vertical profiles of turbulent fluxes (liquid water, water vapor, energy) determine the mean state of the boundary layer and the resulting properties of the Sc deck (Schubert et al., 1979; Bretherton and Wyant, 1997).

Although turbulence is critical to atmospheric boundary layer, microphysical, and large scale cloud dynamics, it is difficult to measure, with literature on describing cloud-related turbulence based on in situ data being scarce (Devenish et al., 2012; Shaw, 2003). One of the major research problems of cloud microphysics remains in being able to understand the fundamental

importance of turbulent processes occurring on extremely small scales, along with gathering in situ data to better understand these turbulent properties (Shaw, 2003). This study therefore aims to characterize turbulence throughout the vertical profile of the Stratocumulus topped marine boundary layer (STBL) over a three-week observation period in October and November of 2008 during the Variability of the American Monsoon Systems (VAMOS) Ocean-Cloud-Atmosphere-Land Study-Regional Experiment (VOCALS-REx). A large in situ dataset was collected throughout the boundary layer, allowing for analysis (on a variety of spatial and temporal scales) in the aims of improving predictions of the Southeast Pacific coupled ocean-atmosphere-land system (Wood et al., 2011). This dataset allows for a classification of turbulent properties not only through vertical profiles, but provides an opportunity to analyze how turbulence changes within the boundary layer with varying synoptic conditions.

The main objectives of this paper include a quantification of the levels amount of turbulence occurring within the boundary layer through the evaluation of turbulent kinetic energy (TKE) dissipation rates, ϵ, and other turbulent flux measurements. In particular, the main goals include: (1) Determine average turbulent values throughout the vertical structure of the STBL, classifying the STBL based on different turbulent profiles analyzed; (2) Analyze day to day variability in turbulent measurements and boundary layer characteristics, relating them to synoptic changes in meteorological conditions.; (2) Determine average turbulent values throughout the vertical structure of the STBL, classifying the STBL based on different turbulent profiles analyzed.

There has been a plethora of publications stemming from the VOCALS-REx campaign over the last ten years. Papers range from focusing on climatic and synoptic conditions for the VOCALS region (Toniazzo et al., 2011; Rahn and Garreaud, 2010a, b; Rutllant et al., 2013), analyzing cloud-aerosol interactions (Jia et al., 2019; Blot et al., 2013; Painemal and Zuidema, 2013; Twohy et al., 2013), and analyzing precipitation, boundary layer decoupling, and other boundary layer characteristics (Jones et al., 2011; Bretherton et al., 2010; Terai et al., 2013; Petters et al., 2013; Zheng et al., 2011), to name a few. A total of five aircraft platforms and two ship based platforms were utilized during VOCALS-REx (Wood et al., 2011), with most publications from VOCALS-REx relying and/or focusing on aircraft observations and other data sources outside of those used here (all but Zheng et al. (2011) and Jia et al. (2019) mentioned above). Results found and presented here therefore provide not only a collection of in-situ turbulent measurements, but provide for the opportunity to relate results to other findings at additional measurement locations within the VOCALS domain. An extensive look at turbulent characteristics of the boundary layer during VOCALS-REx does not exist (note that although Zheng et al. (2011) does give a broad analysis of boundary layer characteristics, their focus on turbulence was minimal), which is puzzling given that the Twin Otter aircraft (the data used here, see Section 2.1) was instrumented with an objective to make turbulence measurements.

Although papers analyzing the overall characteristics of the boundary layer during VOCALS-REx exist (i.e., Zheng et al. (2011)), an extensive look at turbulent properties has yet to be published. A general lack of information on turbulent properties and synoptic scale changes in mean atmospheric conditions is lacking, in particular for marine boundary layers. Analysis of turbulence with changes in synoptic conditions and frontal passages is abundant for locations on land however (i.e., Young and Johnson (1984); Shapiro et al. (1985); Taylor et al. (1993); Frank (1994); Chapman and Browning (2001)). Section 1.1 introduces typical boundary layer vertical structure and scientific background. Section 2 provides an overview of the data and

methods, followed by synoptic and boundary layer characteristics during VOCALS-REx in Section 3. Section 4 will evaluate and discuss the results. Section 5 will provide concluding remarks.

1.1 Boundary Layer Vertical Structure

The vertical structure of the boundary layer is strongly tied to the horizontal and vertical structure of Sc clouds (Lilly, 1968; Bretherton et al., 2010). The STBL is characterized by Sc cloud tops located at the base of an inversion, with subsiding air aloft (as part of the descending branch of the Hadley cell circulation) and well mixed conditions and near-constant conserved variables with height throughout the boundary layer (Wood, 2012). Multiple papers have analyzed typical well mixed STBL vertical structures (i.e., Albrecht et al. (1988); Nicholls (1984)), showing constant potential temperature and mixing ratio with height up until the inversion, when the mixing ratio (potential temperature) sharply decreases (increases). Horizontal winds (both direction and velocity) are typically constant with height throughout the well mixed boundary layer, with changes in both direction and strength typically present at the top of the STBL, influencing cloud-top mixing entrainment (Wood, 2012) (Mellado et al., 2014; Kopec et al., 2016; Schulz and Mellado, 2018).

Convection in the STBL is limited. Unlike updrafts through convective heating over the ground, updrafts within the STBL do not penetrate the inversion. This is because convection within the STBL is primarily driven by cooling near cloud top and not heating at the ocean surface, where cloud top cooling is primarily from a combination of (1) longwave radiational cooling and (2) evaporational cooling from entrainment at cloud top and not heating at the ocean surface. The longwave radiation cools the cloud top, cooling leadings to instability and the convection of warmer, moist air at the surface (Lilly 1968). The cloud cover is greatest when the STBL is shallow [$0.5 < z_i < 1$ km], where z_i is the inversion layer (i.e., boundary layer) height (Wood and Hartmann, 2006).

It is known that clouds are areas of enhanced turbulence (Pinsky and Khain, 1996). Therefore, Sc sheets are turbulent but in contact with an almost non-turbulent upper atmospheric environment. The boundary layer top is characterized by several strong gradients, including the cloud boundary (gradient in liquid water content), the entrainment zone (gradient in vorticity, where the entrainment zone separates regions of weak and strong mixing between laminar (warmer and dryer) flow above and turbulent (cooler and more moist) flow below), and the capping inversion (gradient in potential temperature). The cloud boundary typically lies in the entrainment zone (Albrecht et al., 1985; Kurowski et al., 2009; Malinowski et al., 2013), which in turn lies in the capping inversion, although these layers do not necessarily coincide (Mellado, 2017). Turbulent analysis of these layers in Jen-La Plante et al. (2016) found that turbulence (both TKE and ϵ) decreases moving from cloud top into the free atmosphere above. This results in the entrainment of the upper (laminar flow) layer into the lower (turbulent flow) layer. Through the cloud top entrainment of free tropospheric air as just described, the STBL deepens beyond 1-km and can becomes decoupled. According to Bretherton and Wyant (1997), due to longwave cooling at the cloud top being unable to maintain mixing of the positively buoyant entrained air over the entire depth of the STBL, the upper (cloud containing) layer (turbulence driven primarily by cloud top cooling) becomes decoupled from the surface moisture supply (turbulence driven by surface-fluxes and shear). This process leads to a transition from Sc to cumulus clouds (leading to a subsequent reduction in cloud cover) over the subtropical oceans.

The vertical profile of various turbulent fluxes, particularly that of buoyancy (which is dependent on moisture and heat fluxes which drive buoyancy differences), can tell one a lot about the state of the STBL. For a boundary layer to remain well mixed, the vertical energy and moisture fluxes must be linear functions of height. According to Bretherton and Wyant (1997), the buoyancy flux is not a linear function of height however (unlike that of a dry boundary layer). An increase in the buoyancy flux above the lifted condensation level (LCL) cloud base is typically proportional to the upward transport of liquid water that is required to sustain the cloud against entrainment drying (i.e., continued mixing of the cloud layer is sustained by surface fluxes). Decoupling of the boundary layer (and the subsequent decrease in cloud cover) can occur when the sub-cloud buoyancy fluxes become negative, inhibiting capping convection below cloud base (Albrecht et al., 1988), (Ackerman et al., 2009). According to Shaw (2003), one of the main sources of turbulent kinetic energy (TKE) in clouds is evaporative cooling (due to the entrainment of dry air) and condensational heating (due to droplet condensational growth), implying the buoyancy flux is the primary generator of TKE in the STBL (Schubert et al., 1979) (Heinze et al., 2015). Given this, the buoyancy flux nearly always has a maximum in the cloud layer (Nicholls and Leighton, 1986; Bretherton and Wyant, 1997), with TKE being generated due to longwave and evaporational cooling at cloud top, and condensational heating at cloud base (Moeng et al., 1992). Nicholls (1989) observed through aircraft observations that the largest buoyancy fluxes are close to cloud top, with further observations (Caughey et al., 1982; Nicholls, 1989) suggesting that the descending regions of air originating near cloud top are more a result of radiative cooling rather than evaporative cooling.

The main source of moisture for the STBL is supplied by the surface latent heat flux (LHF), making it an important source of buoyant TKE production (Bretherton and Wyant, 1997), with the surface sensible heat flux (SHF) typically being a much weaker source of turbulence. The sensible heat SHF and latent heat flux LHF can be compared using the Bowen ratio (the ratio of the sensible to the latent heat flux). The smaller the Bowen ratio, the more proportional the liquid water flux in the cloud layer is to the upward moisture or latent heat flux. This results in a A larger latent heat flux LHF (or smaller Bowen ratio) leadings to decoupling of the boundary layer due to the latent heat flux LHF concentrating convective energy generation (through condensational and evaporational heating/cooling) within the cloud layer. To state this another way, an enhanced LHF leads to increased moisture transport to the cloud layer and a thicker cloud, producing more turbulence and enhanced entrainment cooling near cloud top. Enhanced entrainment results in a deepening of the boundary layer, which favors decoupling (Jones et al., 2011). Lewellen et al. (1996) reached a comparable conclusion through assigning shallow stratocumulus layers to preset surface fluxes. This process naturally leads to the buoyancy flux being at a minimum in the sub-cloud layer, priming the boundary layer for decoupling. It is argued in (Bretherton and Wyant, 1997) that the surface latent heat flux LHF is the most important determinant of decoupling within the STBL.

Vertical velocity variance typically displays the strongest updrafts and downdrafts in the upper half of the STBL (Hignett, 1991) (Heinze et al., 2015; Mechem et al., 2012), consistent with the largest production of turbulence being contained within the cloud layer. A positive (negative) vertical velocity skewness indicates that strong narrow updrafts (downdrafts) are surrounded by larger areas of weaker downdrafts (updrafts). It has been found that negative vertical velocity skewness is typically contained within most of the cloud layer and below (Nicholls and Leighton, 1986; Nicholls, 1989) (Mechem et al., 2012) for well mixed boundary layers, whereas a decoupled boundary layer containing cumulus below stratocumulus may contain positive vertical

velocity skewness (de Roode and Duynkerke, 1996) due to convection being driven in the surface layer (as compared to cooling near cloud top). The tendency of the vertical velocity skewness to be positive in a strongly precipitating STBL is also well known (Ackerman et al. 2009), with precipitation being a key contributor leading to boundary layer decoupling (Rapp 2016, Yamaguchi et al. 2017, Feingold et al. 2015).

2 Data and Methods

2.1 Data

Data was collected during the Variability of the American Monsoons (VAMOS) Ocean Cloud-Atmosphere-Land Study-Regional Experiment (VOCALS-REx) from the Peruvian Stratocumulus deck off the west Coast of Chili and Peru during October and November of 2008. VOCALS-REx used various platforms, including five aircraft and two research vessels to accumulate an extensive dataset of the boundary layer, lower free troposphere, and cloud deck along 20°S from 70°W to 85°W. Although multiple sampling platforms, locations, and mission types were deployed during the campaign (see Wood et al. (2011)), data collected by the Center for Interdisciplinary Remotely-Piloted Aircraft Studies (CIRPAS) Twin Otter aircraft will be the focus of this paper, which collected data in the vicinity of 20°S, 72°W; from here on termed Point Alpha. The Twin Otter aircraft was operational for 19 flights from October 16^{th} to November 13^{th}, 2008.

The Twin Otter platform is ideal for a turbulent analysis of the boundary layer due to the aircraft being instrumented to make turbulence and cloud microphysics measurements, with the same location being sampled for each flight. The Twin Otter is also a relatively slow-moving aircraft with a flight speed of roughly 60 ms^{-1}, allowing for a higher resolution of spatial sampling as compared to a faster moving aircraft. Each of the Twin Otter flights was carried out using a stacked flight path (Wood et al., 2011), which involved using stacked legs of 50-100 km in length (horizontal flight paths) to sample various levels of the boundary layer and cloud layer, with at least one aircraft vertical sounding (vertical profile) performed for each flight where the aircraft sampled the free upper troposphere and boundary layer in a single ascent or descent. Each flight of five hours originated from Iquique Chile, allowing for roughly three hours of sampling at Point Alpha.

Of the 19 flights performed by the Twin Otter, only 14 are used here due to instrumentation failure on five of the flights (Phase Doppler Interferometer and the cloud/aerosol probe). Table 1 displays each of the Research Flights (RF) used in this paper. All flights occurred during the day, with all but two flights (RF 8 and RF 17) starting around 7:00 AM local time, with the first vertical profile flown around 8:00 AM local time at Point Alpha. Having each flight sample the same location at roughly the same time is critical, as turbulence typically displays diurnal patterns, with the strongest turbulent mixing occurring during the night when longwave radiational cooling dominates due to the absence of the stabilizing effect of shortwave absorption , which is largest near cloud top due to the scattering of solar radiation limiting absorption lower in the cloud layer at cloud top (Hignett, 1991).

Meteorological variables were collected at 40-Hz (including u, v, and w wind velocity, wind direction, mixing ratio (q) and potential temperature θ), to name a few) while most cloud and aerosol data were collected at 1-Hz. A 5-port Radome wind gust probe was used with plumbing that effectively trapped liquid water, preventing any liquid water from obstructing the

pressure transducer lines. There were zero failures during the campaign, with an accuracy of $\pm$ 0.4 ms^{-1} for horizontal wind components and $\pm$ 0.2 ms^{-1} for vertical velocity. The LI-COR 7500 H_2/CO_2 gas analyzer was used for all measurements of absolute humidity and q, with an ambient air intake setup that resulted in the LI-COR source and detector window to be liquid free, even during prolonged cloud penetrations. The LI-COR accuracy is reported to be within 1% of the actual reading. Further instrumentation information A more in-depth description of the instrumentation used and values measured on the Twin Otter can be found in Zheng et al. (2010) and Wood et al. (2011).

To analyze the synoptic conditions over the study period, data from the National Centers for Environmental Prediction (NCEP) / National Center for Atmospheric Research (NCAR) Reanalysis Project (NNRP, Kistler et al. (2001)) will be used. The data resolution of the NCEP/NCAR reanalysis data is 2.5° x 2.5° x 17 pressure levels, available at six hour intervals. The resolution of this data is suitable for analyzing synoptic scale patterns, but is not ideal for depicting mesoscale variability that may be present from day to day on any given day. Boundary layer height data is also derived from relative humidity data from the European Centre for Medium-Range Weather Forecasts (ECMWF) Re-Analysis (ERA5), which has a resolution is 0.25° x 0.25° x 37 pressure levels, and is available at an hourly interval (Hersbach et al., 2020).

2.2 Turbulent Calculations

The randomness of turbulence makes deterministic description difficult, limiting description to statistics and average values of turbulence, in particular that of Reynolds decomposition (or averaging). Reynolds decomposition uses a mean value (over some time period ,determined by low-pass filtering or applying a linear trend) and subtracts it from the actual instantaneous velocity to obtain the turbulent component (or perturbation value). Reynolds decomposition is based on the underlying assumption that the turbulence is isotropic and stationary, conditions that are hardy fulfilled for atmospheric boundary layer flows however, especially when working with data spanning larger timeframes. The problem is defining how to average collected data to best represent the mean and turbulent components for the fluid flow (with shorter subsets of data having more stationary properties in general than that of longer subsets of data). Using the 40-Hz data, Following the methods outlined in Jen-La Plante et al. (2016), who used a 300-point averaging window, a 320-point averaging window is used here for all turbulent analysis, following the methods outlined in Jen-La Plante et al. (2016). A 320-point averaging window corresponds to 8 second subsets of data (using 40-Hz data), or a roughly 440-m subset of data in the horizontal spatial scale (assuming average aircraft speed of 55 ms^{-1}). Linear regression is then applied to each 320-point averaging window to calculate the mean value and determine the perturbation values.

Applying the averaging method discussed above leads to the calculation of the fluctuations of the u, v, and w components of the velocity, along with other parameters used to measure various turbulent fluxes. Variables to be obtained include turbulent kinetic energy, which is given by:

$$TKE = \frac{1}{2}\left(\overline{u'^2} + \overline{v'^2} + \overline{w'^2}\right) \quad (1)$$

where u', v', and w' are the fluctuations of the velocity components. The turbulent sensible heat, latent heat, and buoyancy fluxes will also be obtained, given by:

$$F_\theta = C_p \overline{\rho} \overline{w'\theta'} \tag{2}$$

$$F_q = L_v \overline{\rho} \overline{w'q'} \tag{3}$$

$$F_{\theta_v} = C_p \overline{\rho} \overline{w'\theta'_v} \tag{4}$$

respectively. Where C_p is the specific heat of air (1005 J kg^{-1}K^{-1}), L_v is the latent heat of vaporization at 20°C ($2.45 \cdot 10^6$ J kg^{-1}), ρ is the mean air density, and θ', q', and θ'_v are the potential temperature, mixing ratio, and virtual potential temperature perturbations, respectively. Note that θ_v (given by $\theta_v = \theta(1 + 0.61q - q_l)$) is commonly used as a proxy for density when calculating the buoyancy. Humid air has a warmer θ_v because water vapor is less dense than dry air, while liquid water drops (if falling at terminal velocity) make the air heavier and therefore associates with a colder θ_v, where q_l is the liquid water mixing ratio.

Just like that of Reynolds decomposition, the calculation of the TKE dissipation rate (ϵ) is based on conditions that the flow is isotropic (i.e., uniformity in all directions), making the measurement of ϵ challenging. In particular, classical turbulence theory in the inertial subrange from Kolmogorov (1941) is based on assumptions of local isotropy. With that said, there are multiple methods to measure the TKE dissipation rate, including the inertial dissipation method, structure functions, and the direct method. Siebert et al. (2006) found that both the inertial dissipation and structure function methods are useful, but the inertial dissipation method sometimes underestimates ϵ at low values due to no clear inertial subrange behavior being observed in the power spectral density, which is not the case for the structure function. The structure function method is therefore considered more robust for cases with small values of ϵ, and will be used here. Due to questions of isotropy, ϵ will be evaluated on the u, v, and w components of the wind, and an average dissipation rate will be calculated from the three components.

The calculation of the dissipation rate ϵ comes from the analysis of the velocity perturbations through the nth order structure functions (i.e., a statistic to analyze common variation in a time series). The perturbations, as for other turbulent parameters, are determined with respect to an averaging window of 320-points. Each subset of perturbations is then appended to the end of the previous subset to create a single time series of velocity perturbations. The structure function is given by:

$$S_n(l) = \left(\overline{|u(x+l) - u(x)|}\right)^n \tag{5}$$

where l is the distance (or in the case of a temporal series, l is equivalent to t assuming constant flight speed). From Frisch (1995), the dissipation rate using the nth order structure function can be obtained by using:

$$S_n(l) = C_n |l\epsilon|^{\frac{n}{3}} \tag{6}$$

where C_n is a constant of the order 1. The second order structure function will be used here ($n = 2$), where C_2 is equal to = 2 for transverse velocity fluctuations and C_2 is equal to = 2.6 for longitudinal velocity fluctuations (Chamecki and Dias, 2004), where vertical fluctuations are considered transversal and horizontal fluctuations (both u' and v') are considered longitudinal, following the methods in Jen-La Plante et al. (2016). The structure function follows a $2/3$ power law within the inertial subrange

and will only be used to calculate the dissipation rate between frequencies of 0.3-5-Hz, neglecting the higher frequency features attributed to interactions with the plane (i.e., vibrations due to the aircraft) and other instrumental artifacts.

Figure 1 Panel (a) provides the power spectral density of vertical velocity and q for three horizontal flight legs within RF3, one in-cloud, one sub-cloud, and one near surface. Note that the power spectral density follows a -5/3 power law fit (red) within the inertial subrange (as opposed to the 2/3 power law fit of the structure function). A spike in energy can be seen at $\sim$10-Hz, which represents the aircraft interactions discussed previously. The power spectral density overlaid in black represents a single calculation using a 320-point averaging window. The data follows the -5/3 fit well, and the inertial subrange is well resolved for the averaging window used (with the light gray envelope representing the 0.3 to 5-Hz range). A lack of significant flattening within the power spectra at higher frequencies suggests that the random noise level is low (this is more evident in the vertical velocity spectra than that of the q spectra).

Analysis of the turbulence as presented here introduces two types of error, including sampling and noise error. This must be analyzed to determine the statistical significance when analyzing vertical profiles, especially since error propagation into higher order moments can be significant (McNicholas and Turner, 2014). Sampling errors were estimated using approaches derived and discussed in Lenschow et al. (1994, 2000) and will not be repeated here. Noise error must be considered, as noise within the instrumentation may be significant enough that the atmospheric component of the variance is small compared to the overall measured variance. Noise is measured using the extrapolations of the measured autocovariance functions to lag 0 by the structure function. This technique was introduced in Lenschow et al. (2000) to estimate the noise contribution from the second to fourth order moments. Although this technique was traditionally used to estimate lidar noise (Wulfmeyer, 1999; Wulfmeyer et al., 2010, 2016), it has also been extended to in-situ observations (Turner et al., 2014).

Figure 1, Panel (b) provides the autocovariance function of vertical velocity and q for a sub-cloud fight leg in RF3 (black). The fit using the structure function is provided in red (vertical velocity) and green (q). The structure function at lag zero provides the mean variance, while the difference between the autocovariance and structure function at lag zero provides the system noise variance at the corresponding temporal resolution. It is clear that the atmospheric variance and noise can be separated. For example, from Panel (b), looking at the vertical velocity, $\overline{w'^2}$= 0.20 m^{2}s^{-2} and the noise variance $\overline{\delta_w^2}$ = 0.014 m^{2}s^{-2}. This results in a noise standard deviation of δ_w = 0.12 ms^{-1}.

Extending this analysis to determine the error propagation within higher order moments, error bars for vertical velocity variance and q variance, vertical velocity skewness, and the kinematic moisture flux $w^{'}q^{'}$ can be found in Panels (d) through (f), respectively, with noise error bars in red and sampling error bars in black. The noise error is negligible compared to the sampling error, in agreement with results from Turner et al. (2014). Note that some data points do not have noise error bars associated with them. This is due to the fact that the noise was so small, the error bars would not plot. The various vertical profiles displayed show that the sampling errors result in a lack of statistical significance between flight legs of different altitudes.

Equations used to determine the noise in the higher order moments from Wulfmeyer et al. (2016) are:

$$\sigma_{w'^2} \cong 2\sqrt{\overline{w'^2}}\sqrt{\frac{\delta^2}{N}} \tag{7}$$

$$\sigma_{w'^3} \cong 3\sqrt{3\overline{w'^2}}\sqrt{\frac{\delta^2}{N}} \tag{8}$$

$$\sigma_{w'q'} \cong \sqrt{\overline{q'^2}\frac{\delta_w^2}{N} + \overline{w'^2}\frac{\delta_q^2}{N}} \tag{9}$$

where N is the number of data points. Using this, the absolute error for the vertical velocity variance is found to be 0.00068 m^2s^{-2} and the relative error is 0.35% (the relative error for the q variance is 1.9%). Both errors are very reasonable, and demonstrate the low noise of the instrumentation.

3 Synoptic and Boundary Layer Characteristics

3.1 Mean Synoptic Conditions

The Southeast Pacific Ocean is found on the eastern edge of the south-Pacific semipermanent subtropical anticyclone, characterized by large scale upper tropospheric subsidence leading to a strong temperature inversion with a well-mixed boundary layer below. The surface pressure therefore is controlled in part by the location of the south-Pacific subtropical anticyclone. This anticyclone is routinely interrupted (especially between fall and spring) by periods of relative low pressure which is associated with localized troughing or the passage of midlatitude cyclones to the south. Several papers (Toniazzo et al., 2011; Rahn and Garreaud, 2010a) have analyzed the synoptic characteristics during VOCALS-REx, these papers however tend to focus on the VOCALS-REx region as a whole, and not specifically on Point Alpha, which is done in this section.

Figure 2 shows the mean of large-scale meteorological conditions, (including sea level pressure, omega (ω, representing vertical velocity in pressue coordinates), and 700-hPa geopotential height) from NCEP reanalysis data over the study region between October 19^{th} to November 12^{th}. The mean sea level pressure (panel (a)) displays the anticyclone near it's climatological position of 30°S, 100°W (Toniazzo et al., 2011). The overlaid sea level pressure standard deviation (only displayed up to 20 hPa) shows variability increasing southward, indicating enhanced midlatitude storm tracks. Enhanced variability that is in line with midlatitude troughing from panel (b) also decreases toward the coast, suggesting more variation in the synoptic pattern over the open ocean as compared to the near-coastal region. This is as expected, as Barret et al. (2009) found that synoptic systems tend to weaken as they move towards the coast of South America.

The mean 700-hPa geopotential height is displayed in panel (b), overlaid with omega ω data. Subsidence (green shading) dominated the VOCALS-REx region, with Point Alpha having an average value of 0.066 Pa s^{-1} 57 hPa day^{-1} at the 700-hPa

level. While enhanced storm tracks were primarily contained within the mid-latitudes, the 700-hPa geopotential height displays midlatitude troughing extending between Point Alpha and the subtropical high (as was found in (Zheng et al., 2011)), suggesting that meteorological conditions at Point Alpha were influenced by both midlatitude synoptic systems and the subtropical anticyclone.

The sea-level pressure was also measured using both reanalysis data and aircraft 30-m level horizontal flight legs. Figure 3, panel (a) shows that the reanalysis data at Point Alpha tended to be on average 1.5-hPa greater than the aircraft measured sea level pressure. The pressure decreased by roughly 3-hPa from October 19^{th} to November 12^{th}, however, this decrease cannot be considered a seasonal signal because it is within synoptic scale variation. The sea surface temperature (SST) and atmospheric surface temperature (both measured during 30-m horizontal flight legs) increased steadily throughout the observation period, increasing by 2.79 and 2.28 °C, respectively.

3.2 Synoptic Variability at Point Alpha

Synoptic variability at Point Alpha is summarized by time series of geopotential height at various levels. Higher geopotential heights are associated with ridging aloft while decreases in geopotential heights are associated with synoptic disturbances or troughs. The 500-hPa geopotential height (see Figure 3) varied between 5840 and 5900-hPa m, with an increase of 9-hPa m between October 19^{th} and November 12^{th}. Figure 3 also displays enhanced synoptic scale variation during October, with several disturbances effecting Point Alpha. The 500, 700 (panel (c)), 850, and 1000 (panel (d)) hPa geopotential heights alternate between areas of high and low height through November 2^{nd}. After November 2^{nd}, the 500-hPa geopotential height is more consistent, with height increasing over Point Alpha until November 10^{th}, at which point the height begins to decrease.

Besides minor disturbances in October, there are two main disturbances that stand out. The first disturbance occurs on November 1^{st} and 2^{nd} (green shading in Figure 3), where both the 500 and 700-hPa heights have minimums (5842 and 3134 m, respectively). The 850 and 1000-hPa heights also have secondary minimums. The second disturbance was the formation of a costal low, which can be seen by decreasing geopotential heights on November 12^{th}. Both the 850 and 1000-hPa geopotential heights reached minimums on November 12^{th} (1498 and 104 m, respectively). This costal low reached a minimum (the coastal low was strongest) after the analysis period, on November 15^{th} (Rahn and Garreaud, 2010a). The ridging which formed after November 2^{nd} leads to the formation of the coastal low through the warming of the lower and middle troposphere (Garreaud and Rutllant, 2003).

How the boundary layer turbulence changed with the synoptic evolution, particularly the disturbance observed on November 1^{st} and 2^{nd}, will be the focus of this paper. The 700-hPa geopotential height map (not shown here) displayed a midlatitude trough developing and extending past Point Alpha from October 29^{th} through November 3^{rd}, as is shown in Figure **??**. A deep midlatitude trough forms off the west coast of South America by October 30^{th}, extending past 15°S. The trough axis begins to move over Point Alpha by October 31^{st}, with the main impacts of the trough on Point Alpha (in terms of lowest geopotential height) being observed on November 1^{st} and 2^{nd}. The 500-hPa geopotential height map (not shown here) shows the ridge axis directly over Point Alpha on November 1^{st}.

Figure 4 (panels (a) through (c)) show atmospheric wind direction and velocity using data collected from horizontal flight legs. Panel (d) and (e) displays wind direction and wind speed using data collected from aircraft vertical soundings. Atmospheric winds near the surface (measured during 30-m horizontal flight legs) at Point Alpha were mostly southerly (150 to 180°) with a mean of 176°. Strong wind shear was present near the inversion, with winds above the marine boundary layer (measured during horizontal flight legs above the inversion) having a mostly northwesterly component (mean of 273°) while having more variability in direction than that of the boundary layer (300 to 360°). Although on most flight days the winds speed and direction were mostly constant with height in the boundary layer (see panel (d) and (e)), on November 1^{st} and 4^{th} (blue lines) the wind direction shifted sharply within the boundary layer from southerly to northeasterly along with varying wind speed. On November 2^{nd} (green line), the wind direction had its strongest westerly component (214°). Shear within the boundary layer is not common. Zheng et al. (2011) suggest that this shear is linked to coastal processes such as the propagation of the upsidence wave. It should also be noted however that the wind shear within the boundary layer is present on the same day (November 1^{st}) that the trough axis is located over point alpha. On the proceeding day, the surface winds experience their most westerly component. According to Rahn and Garreaud (2010a), as troughs approach the coast of South America, southeast winds are typically replaced by southwest winds. Between October 29^{th} and November 2^{nd}, wind direction within the boundary layer shows its most variation, gradually shifting from 153° (most easterly component measured) to 213° (most westerly component measured), respectively. While the trough approaches the coast of Chile, southeast winds are replaced by southwest winds, as is typical of synoptic scale disturbances in the region (Rahn and Garreaud, 2010a).

3.3 Boundary Layer Characteristics

Boundary layer height is perhaps the most important feature of the marine boundary layer (MBL), with the height z_i being one of the main dictators for boundary layer characteristics such as decoupling and cloud cover (Albrecht et al., 1995). Findings from Rahn and Garreaud (2010a) at a separate observation point within the VOCALS-REx region suggests that the boundary layer depth z_i tended to be either low (600-m) or high (1500-m) with periods of high or low depth interrupted by rapid transitions between the two states over 12 to 36 hour periods due to synoptic variability. Figure 5 shows the thickness of the Sc cloud layer, the thickness of the inversion layer (entrainment zone), and subsequently the MBL height for each flight. The expected lifted condensaton level (LCL) for a well mixed boundary layer is also provided, using $z_{LCL} = 123(T - T_d)$, where T_d is dew point temperature. MBL height z_i is also provided from extrapolating relative humidity using data from ECMWF reanalysis (Engeln and Teixeira, 2013). The cloud layer was identified using a liquid water content (LWC) greater than or equal to 0.01 g m^{-3}, while the inversion layer was identified by the region of greatest change in the mixing ratio q (absolute change $\geq$ |0.10 g kg^{-1}| per measurement) and potential temperature θ (absolute change $\geq$ |0.20 K| per measurement) within the vertical profiles. This results in the bottom of the inversion layer characterized by the profiles beginning to lose the boundary layer features, while the top of the inversion layer had lost all boundary layer features.

The average height of the boundary layer z_i was 1175-m (see Table 2 for boundary layer characteristics), with the average cloud layer and inversion thickness being 239 and 59-m, respectively. The sharp inversion layer suggests that the interaction between boundary layer and free tropospheric air aloft extended over a relatively thin layer. Figure 5 shows that the boundary

layer height z_i varied between 996 and 1450-m, with mostly gradual changes in height from flight day to flight day (note that the mean difference between z_i and ECMWF-z_i was 43 $\pm$ 26-m). The average change in boundary layer height z_i (in regards to the in situ data) was 68 m day^{-1} with four occurrences of a rate of change above 100 m day^{-1}. After October 27th is when the most significant changes took place to the cloud thickness and boundary layer height z_i. Between October 27th and 29th (no flight day in-between), the boundary layer height z_i increased from 995 to 1300-m (152 m day^{-1}, the second largest rate of change),where the ECMWF-z_i shows that the increase was mostly confined from October 27th to October 28th. The next four flight days recorded the thickest cloud layers, peaking on November 1st and 2nd with thicknesses of 382 and 472-m, respectively. It should also be noted that between October 29th and 30th, the boundary layer height z_i decreased from 1300 to 1177-m (124 m day^{-1}, the third largest rate of change, although this is not conveyed in the ECMWF-z_i data). After November 2nd, the cloud layer thinsed and the boundary layer height z_i increased from 1136-m to 1450-m between November 4th and November 8th. Although this is a rate of 79 m day^{-1}, there is no in situ data in-between November 4th and 8th. The ECMWF-z_i provides a mean rate of change for this period of 93 m day^{-1}, with the largest change of 160 m day^{-1} between November 7th and 8th, suggesting a rapid rise in z_i, in concurrence It is unknown whether the boundary layer height increased rapidly over a day or two (as would be expected from findings in Rahn and Garreaud (2010a), or gradually increased day over day in-between flights. After the boundary layer height z_i peaks on November 8th, the boundary layer height falls rapidly over the next two days, showing decreases of 174 m day^{-1}and 102 m day^{-1} from November 8th to November 10th, respectively.

Although the time series of cloud droplet number concentration is not shown here, it showed a notable dip to a minimum on November 1st of 81 cm^{-3} (where the average is 292 cm^{-3}), corresponding with minimums in both boundary layer cloud condensation nuclei and aerosol number concentration. Above boundary layer aerosol number concentration both had a maximum on November 1st. However, this can most likely be attributed to enhanced moisture (see Figure 6) above the boundary layer due to the passing synoptic system, where enhanced moisture can increase the size of hygroscopic aerosols that would otherwise be too small to be measured under dryer conditions.

Figure 6 shows vertical profiles (where the height (z) is normalized with the inversion height to give a non-dimensional vertical coordinate of z/zi) (based on a normalized boundary layer height) of potential temperature θ, mixing ratio q, liquid water content LWC, and the aerosol number concentration. Individual flight profiles are in gray, with the red profile representing the mean and the blue profiles representing the flights conducted on November 1st (RF11) and November 2nd (RF12). Mean profiles show that on average the MBL is well mixed up to the inversion, which then prevents mixing into the free atmosphere above (as evident by the decrease in aerosol number concentration between the boundary layer and free atmosphere above).

The largest deviations from the mean in the profiles occur during the passage of the synoptic system on November 1st and 2nd. At this time, both RF11and RF12 measured (1) The thickest Sc cloud layer, with November 1st having the largest average cloud droplet size (20.8 μm) and in-cloud drizzle rates, while November 2nd had the lowest recorded cloud base and largest recorded liquid water content LWC; (2) The largest A larger mixing ratio above the boundary layer. This suggests the presence of a moist layer aloft which may have helped in producing the thickest cloud layers observed; (3) The smallest differences in both potential temperature θ and mixing ratio q from the bottom to the top of the inversion layer. During the passage of strong events as described by Rahn and Garreaud (2010a), the inversion defining the MBL erodes, making it hard to define the

boundary layer height z_i. This process is partially displayed by the small differences in temperature and moisture across the inversion layer during the passage of the synoptic disturbance.

The differences in mixing ratio q and potential temperature θ can be better visualized in Figure 7, which shows the differences between below and above inversion values in panel (ba). Data between normalized boundary layer height z/z_i values of between 0.85 and 0.95 were used for the averages below the inversion, while data between normalized altitude z/z_i values of 1.10 and 1.20 were used for the averages above the inversion. Besides November 1^{st}, 2^{nd}, and to a lesser degree November 4^{th}, the average difference in potential temperature θ across the inversion was 17-K, while the average difference in mixing ratio q was -6.2 g kg^{-1}. On November 1^{st} when both reached a minimum difference, the difference between the mixing ratio q and potential temperature θ across the inversion was 1.9 g kg^{-1} and 14-K, respectively, where a weaker inversion allows for more entarinment mixing near cloud top (Galewsky, 2018).

There are multiple methods which can be used to analyze whether the boundary layer is well mixed or decoupled. Methods used here include (1) decoupling parameters and (2) analysis of the expected LCL for a well-mixed layer in relation to actual cloud base. Decoupling parameters α_θ and α_q depend on the profiles of θ and q, respectively (Wood and Bretherton, 2004). Analyzing wheather the boundary layer is well mixed or not (as displayed in Table 1) based on potential temperature and mixing ratio can be quantified using the decoupling parameters α_θ and α_q, respectively (Wood and Bretherton, 2004).

The decoupling parameters measure the relative difference in mixing ratio q and potential temperature θ between the bottom (near the surface) and top (near the inversion) portions of the boundary layer, and are given by:

$$\alpha_\theta = \frac{\theta(z_i^-) - \theta(0)}{\theta(z_i^+) - \theta(0)} \tag{10}$$

$$\alpha_q = \frac{q(z_i^-) - q(0)}{(z_i^+) - q(0)}, \tag{11}$$

where z_i^+ (z_i^-) is the level ~25 m above (below) the inversion z_i, and $\theta(0)$ and $q(0)$ are the potential temperature and mixing ratio at the surface. Here, z_i^+ is calculated using data between normalized boundary layer heights z/z_i values of 1.03 to 1.05, while z_i^- is calculated using data between normalized boundary layer heights z/z_i values of 0.95 to 0.97 (this is roughly 25 m above and below the inversion z_i, respectively). The closer to zero the decoupling parameters are, the more well-mixed the boundary layer is. Previous observations suggest that if the parameters exceed $\sim$ 0.30, the boundary layer is decoupled (Albrecht et al., 1995).

Mixed layer cloud thickness represents the difference between z_i and the LCL (Δz_m), and was found to be strongly correlated to decoupling in Jones et al. (2011). The difference between cloud base (z_b) and the LCL represents another decoupling index (Δz_b) related to the LCL presented in Jones et al. (2011). Decoupling of the boundary layer occurs when the boundary layer deepens, resulting in a larger difference between the inversion and the LCL as the LCL diverges from cloud base. A well-mixed boundary layer would have z_b and LCL measurements which are in close agreement, while a decoupled boundary layer would have a divergence in the similarities between the two values. Previous observations within the VOCALS-REx domain from Jones et al. (2011) found that the boundary layer tended to be decoupled if Δz_b > 150-m and if Δz_m > 500-m.

Figure 7 shows the decoupling parameters in panel (ab). The average value of α_θ (α_q) is 0.15 (0.07), both which are within the regime of well mixed. During RF11 and RF12 the mixing ratio q increases above the inversion leading to large values for α_q, while the potential temperature change $\Delta\theta$ is relatively small as compared to other flights, with α_θ being above 0.30 during November 1^{st}, where Zheng et al. (2011) suggest drizzle processes act to stabilize the boundary layer, leading to decoupling on November 1^{st}. Panel (c) provides values for Δz_b and Δz_m for each flight, with average values of 125 and 363-m, respectively. Again, both values are within the regime of well mixed. RF11,13, and 15 are shown to be decoupled, with both Δz_b and Δz_m at or above the 150 and 500-m threshold values, respectively. RF12 is decoupled according to Δz_m only. Looking at raw profiles of q and θ (not shown here), RF11, 12, 13, and 15 appear to be decoupled due to distinct humidity changes within the sub-cloud profiles, including the presence of a cumulus layer below the Sc deck that is visible from analyzing the LWC profiles (not displayed here) during RF11 (November 8^{th}). This results in 28% of profiles analyzed being decoupled. Although on November 8^{th} both parameters are below 0.30, the boundary layer is decoupled due to the presence of a secondary cloud cumulus layer below the Sc deck that is visible from analyzing the LWC profiles.

The comparison between Panels (b) and (c) demonstrate that determining decoupling using Δz_b and Δz_m appears to be more accurate than the decoupling parameters when comparing the results to the raw vertical profiles. A more accurate value for determining decoupling using α_θ and α_q for the data presented here is 0.20, as compared to the 0.30 stated in Albrecht et al. (1995). A value of 0.20 would lead to better agreement between the two methods. Note that the correlation between α_θ and α_q is 0.79 (i.e., when the mixed layer cloud thickness increases, the difference between the LCL and cloud base increases). This suggests that when the boundary layer deepens, the cloud layer remains relatively consistent, in agreement with findings from Jones et al. (2011).

4 Results

The vertical variation in turbulent properties and fluxes can be conveniently discussed in terms of dividing the boundary layer into vertical layers. Here, we will quantify the amount of turbulence occurring within the boundary layer. In particular, analysis includes: (1) Determine average turbulent values throughout the vertical structure of the STBL, classifying the STBL based on different turbulent profiles analyzed; (2) Analyze day to day variability in turbulent measurements and boundary layer characteristics, relating them to synoptic changes in meteorological conditions; (2) Determine average turbulent values throughout the vertical structure of the STBL, classifying the STBL based on different turbulent profiles analyzed. For each flight analyzed here, the Sc deck lies directly below a strong inversion. This extreme vertical gradient can cause instrument response issues with the measurement of both the dry bulb and dew point temperature for some distance beneath cloud top (Nicholls and Leighton, 1986). Therefore, data collected during both vertical profiles and horizontal legs will be used and compared.

4.1 Synoptic Variability of Turbulence

Figure 8 shows the mean surface (30-m horizontal flight leg) latent heat flux LHF (panel (a)), sensible heat flux SHF (panel (b)), and Bowen ratio (panel (c)) for each flight day with the standard deviation represented by the gray envelope. Note that for days with two or more mean values, there were two or more 30-m horizontal flight legs, with good agreement between mean leg values within the same flight. The latent heat flux LHF peaks on Oct 26^{th} with a value of 53.3 W m^{-2}, and from that point decreases steadily to its minimum values of 19.7 and 18.5 W m^{-2} just as and after the minimum in geopotential height on Nov. 2^{nd} and 4^{th}, respectively. The sensible heat flux SHF has a sharp increase to its maximum value of 17.1 W m^{-2} on Nov 1^{st} and decreases to its secondary minimum on Nov. 2^{nd} (note that mean values of surface fluxes can be found in Table 3). The Bowen ratio is typically small (less than 0.20), especially for the first half of the campaign. The Bowen ratio has a sharp increase on Nov 1^{st} to match the increase in the SHF latent heat flux (and remains above 0.20 for the remainder of the analysis period), suggesting that the liquid water flux in the cloud layer should not be taken to be proportional to the upward latent heat flux LHF after Nov 1^{st}. Note that the average surface values of LHF and SHF are generally in agreement with those found in Zheng et al. (2011), who found values of 48.5 and 7.1 W m^{-2}, respectively. The differences most likely arise due to different averaging techniques.

Figure 9 gives the surface friction velocity (vertical transport of horizontal momentum), vertical velocity variance, TKE, and the TKE dissipation rate ϵ in Panels (a) through (d), respectively. One commonality between each parameter is that the maximum value is reached on Nov. 1^{st} followed by the minimum value on Nov. 2^{nd} (see Table 3 for the mean and range of the values). For all four variables, there is very little variation between measurements, except for between Oct 30^{th} and Nov 2^{nd}, where a large increase in turbulence is observed before a rapid decrease. Overall, there is good agreement between mean values for the same flight, with the exception of Nov 12^{th}, which contains the largest difference between mean values for each variable in discussion here. This large difference was not observed however for the surface latent LHF and sensible heat flux SHF. Note that the average surface values of latent and sensible heat are generally in agreement with those found in Zheng et al. (2011), who found values of 48.5 and 7.1 W m^{-2}, respectively. The differences most likely arise due to different averaging techniques.

Shifting focus to the entire depth of the boundary layer, Figure 10 shows boxplots (made up of leg mean values) of subbelow-cloud (white) and in-cloud (blue) values of latent heat flux LHF (Panel (a)) and buoyancy flux (Panel ((c)). Panels (b) and (d) display histograms of the latent heat flux LHF and buoyancy flux data with normal distribution fits for reference, respectively. The overall latent heat flux LHF was 11.03 $\pm$ 12.97 Wm^{-2}, with the subbelow-cloud mean being 15.74 $\pm$ 16.4 Wm^{-2} and the in-cloud mean being 6.01 $\pm$ 3.75 Wm^{-2}. The subbelow-cloud latent heat flux LHF is clearly offset to larger values, owing to surface evaporation and subsequent transport of moisture. The red dots in Panel (a) represent the surface values, which are always the largest within the entirety of the vertical layer. The lowest mean values occurred on the same days as the minimum in geopotential height, Nov 1^{st} and 2^{nd}, with values of 5.51 and 4.67 Wm^{-2}, respectively. Although these two data sets are visually different, statistically speaking they are similar, with a p-value of 0.22 (note that all statistical significance testing will be carried out using the Wilcoxon-Sum-Rank-Test).

The buoyancy flux in Panel (c) displays that the overall mean buoyancy flux was 4.89 ± 4.86 Wm^{-2}, with the subbelow-cloud mean being 4.64 ± 3.94 Wm^{-2} and the in-cloud being 5.12 ± 5.64 Wm^{-2}. From just analyzing the mean values of flight legs, there does not appear to be a large difference in the buoyancy flux between the subbelow-cloud and in-cloud sections of the boundary layer, which is not as expected. In-cloud buoyancy in general is enhanced due to latent heating and cooling effects. There is no statistical significance between the in-cloud and subbelow-cloud data, with a p-value of 0.39. While the medians in the data populations are similar, the buoyancy flux in-cloud has a much larger range, suggesting isolated occurrences of extremely large buoyancy fluxes within the cloud. Connecting back to concepts discussed in the introduction, the coefficient correlation between the surface latent heat flux LHF and the in-cloud buoyancy is 0.40, suggesting some evidence that a larger surface latent heat flux LHF leads to a larger in-cloud buoyancy flux, as suggested by Bretherton and Wyant (1997) and Lewellen et al. (1996).

Figure 11 displays provides the same information format as that of Figure 10, except for TKE (Panel (a)) and TKE dissipation ϵ (Panel(c)). The total mean TKE was 0.132 ± 0.03 m^{2}s^{-2}, with a subbelow-cloud mean of 0.133 ± 0.05 m^{2}s^{-2} and an in-cloud mean of 0.132 ± 0.04 m^{2}s^{-2}. The total mean ϵ was 3.97 ± 1.28 cm^{2}s^{-3}, with a subbelow-cloud mean of 4.14 ± 2.45 cm^{2}s^{-3} and an in-cloud mean of 3.80 ± 1.81 cm^{2}s^{-3}. Overall, very consistent values (when looking at the means) between subbelow-cloud and in-cloud exist, resulting in statistical similarity between the data populations for both TKE and ϵ. However, in looking at the boxplots, one can see that there are several cases (including Nov 1^{st} and Nov 2^{nd}) where the entire turbulent distribution of the subbelow-cloud data is shifted to larger values than those of in-cloud data, with minimal overlap. This implies that the two layers have limited mixing between them, perhaps due to a more turbulent decoupled lower boundary layer. This will be explored in further detail in Section 4.2. Along with having different turbulent distributions between in-cloud and subbelow-cloud, both the TKE and the ϵ had maximum values on Nov 1^{st} (0.163 m^{2}s^{-2} and 6.13 cm^{2}s^{-3}, respectively) and minimum values on Nov 2^{nd} (0.065 m^{2}s^{-2} and 1.30 cm^{2}s^{-3}, respectively).

The analysis to this point clearly shows a maximum in turbulent properties on Nov 1^{st} and a minimum on November 2^{nd}. This maximum is driven from turbulence below the cloud however, with the in-cloud TKE (0.128 m^{2}s^{-2}) and ϵ (2.78 cm^{2}s^{-3}) being below normal for in-cloud values, where the normal is 0.129 m^{2}s^{-2} and 3.68 cm^{2}s^{-3}, respectively. Panel (d) shows the total ϵ distribution for in-cloud and subbelow-cloud. An increase in in-cloud frequency for ϵ is clear for the lowest values (first two histogram bars). Eight of the 15 measurements from the first two histogram bars came from RF11 and RF12 (Nov 1^{st} and Nov 2^{nd}), which includes all in-cloud values for those flights. The other seven measurements were all sampled above a normalized boundary layer height of $z/z_i = 0.90$, suggesting entrainment mixing of stable more laminar flow from the upper atmosphere near the top of the entrainment layer into the upper cloud layer boundary layer, reducing the turbulent energy.

It is important to analyze turbulent fluxes of energy, momentum, and moisture as they act to determine boundary layer structure and characteristics, along with analyzing how these variables are related to synoptic scale properties such as geopotential height. The correlation coefficients between boundary layer characteristics and synoptic scale properties can be found in Table 4. The 700-hPa geopotential height (i.e., pressure) is fairly correlated with the boundary layer height, although this correlation is negative with a value of -0.37, suggesting that as the geopotential height pressure increases, the boundary layer height

decreases. The rate of change in the boundary layer height z_i can be governed by:

$$\frac{dh}{dt} = \omega_e + \overline{\omega} \tag{12}$$

where h is boundary layer height, ω_e is the entrainment rate (ω_e) and ω is the synoptic scale vertical velocity (positive upwards). This suggest that. If the rate of subsidence increases to the point that it is larger than ω_e , then the boundary layer height will decrease with time. ω depends primarily on synoptic scale patterns, in particular that of geopotential height. Pressure and ω have a correlation of -0.89, suggesting that as pressure increases, the subsidence increases (or at the very least, upward vertical motion is diminished). Entrainment on the other hand, can depend on multiple variables including the inversion layer thickness, wind shear, and surface fluxes. Increases in ω_e result in a higher LCL However, periods of ridging which lead to stronger synoptic scale subsidence aloft will also act to increase entrainment, resulting in a higher lifted condensation level (LCL) for the entrained air, and a resulting increase in boundary layer height as a result. Given that h z_i acts to decrease as the geopotential height pressure increases, this suggests that the subsidence becomes the dominating component that governs h z_i over that of entrainment. The correlation between entrainment zone thickness and the boundary layer height is 0.22, in other words, as the geopotential height increases, both the boundary layer and the entrainment zone thickness decreases, and vice versa. Both TKE and ϵ increase in-cloud with respect to the geopotential height (correlation coefficient of 0.23 and 0.24, respectively) and decreases with respect to boundary layer height (-0.32 and -0.34, respectively).

The surface LHF provides the main source of moisture in the STBL, which in turn is an important source of buoyant TKE production. An enhanced (reduced) LHF will generate thicker (thinner) clouds with larger (smaller) LWC values, resulting in enhanced (reduced) evaporative cooling near cloud top leading to enhanced (reduced) buoyancy driven entrainment, and a subsequent deepening (thinning) of the boundary layer. This process is demonstrated well when analyzing the correlation coefficients. Both the LHF and SHF are positively correlated with z_i (correlation coefficients of 0.36 and 0.44, respectively) while the LHF is negatively correlated with the Sc cloud thickness (correlation coefficients of -0.50). Therefore, a larger LHF tends to result in a thinner Sc cloud layer but a larger z_i, suggesting enhanced entrainment which acts to thin the cloud layer while deepening the boundary layer. It should also be noted that the correlation between the SHF and wind speed is significant, as anticipated since the SHF is expected to increases linearly with wind speed (Palm et al., 1999).

Both TKE and ϵ increase in-cloud with respect to pressure (correlation coefficient of 0.23 and 0.24, respectively) and decreases with respect to z_i (-0.32 and -0.34, respectively). The observed decrease in boundary layer turbulence with increasing z_i is due to decoupling and an inability for the entire boundary layer to be mixed (leading to a subsequent decrease in turbulence), while a shallow boundary layer can be easily mixed through cooling at cloud top.

As the cloud droplet number concentration and aerosol number concentration increase (accompanied by a decrease in average droplet size), the TKE and ϵ increase (with correlation coefficients of 0.35, 0.42, and -0.32 in relation to TKE, respectively). Physically this makes sense, as precipitation is suppressed due to larger number concentrations and smaller droplet sizes, a reduced moisture loss from the STBL can result, leading to thicker clouds, a larger buoyancy flux, and a larger TKE. Smaller droplets will also evaporate more readily, leading to enhanced latent heating effects and a resultant increase in turbulence. The correlation between the sensible heat flux and wind is the largest, with a value of 0.64, as expected since the sensible heat flux

is expected to increase linearly with wind speed. The correlation between the boundary layer height and sensible heat flux is 0.36.

To summarize, the correlation coefficient values found here imply that the sensible heat flux is strongly correlated with wind speed, boundary layer height, and geopotential height, in agreement with Palm et al. (1999). It is found that as the boundary layer height decreases, TKE and ϵ tend to increase, along with the sensible and latent heat flux. The increased geopotential height (or decrease in boundary layer height), which is most strongly correlated with the sensible heat flux (0.56 and 0.49 for in-cloud and below-cloud, respectively), leads to enhanced values of sensible and latent heat and stronger turbulent values. The various correlation coefficients indicate that (1) as the geopotential height decreases, the boundary layer height and entrainment zone increase, accompanied by a decrease of in-cloud and below-cloud turbulence; (2) as the geopotential height increases, the boundary layer height and entrainment zone decrease, accompanied by an increase of in-cloud and below-cloud turbulence. The observed decrease in boundary layer turbulence with increasing boundary layer height could be due to decoupling and an inability for the entire boundary layer to be mixed (leading to a subsequent decrease in turbulence), while a shallow boundary layer can be easily mixed through cooling at cloud top.

4.2 Vertical Profiles

It has been shown through the boundary layer vertical structure in Figure 6 that the boundary layer is, on average, well mixed when considering thermodynamic variables. Figure 12 represents vertical profiles of the buoyancy flux (Panel (a)), latent heat flux LHF (Panel (b)), vertical velocity variance (Panel(c)), and TKE (Panel (d)), where each dot represents a leg mean value, with in-cloud values in red and values measured during Nov 1^{st} and Nov 2^{nd} in blue. The buoyancy flux in the sub-cloud layer (on average) varied between -2 and 20 Wm^{-2} and decreased with height until increasing within the cloud layer with values ranging between -5 and 43 Wm^{-2}. The standard deviation (in orange) was produced using data from vertical flight profiles as opposed to the horizontal legs due to data uniformity throughout the boundary layer depth. The buoyancy flux has a clear increase in variance within the cloud layer. The latent heat flux LHF peaks near the surface, ranging between -1 and 55 Wm^{-2} below the cloud layer and generally decreases with height. The variance peak of 33 Wm^{-2} occurs at a normalized boundary layer height of z/z_i 0.99, displaying signifying the large gradient in q near z_i and the variation in evaporative cooling due to entrainment mixing at cloud top between flight days.

Vertical velocity variance (from here on $\overline{w'w'}$) ranged from 0.008 to 0.20 $\mathrm{m}^2\mathrm{s}^{-2}$. The observed in-cloud $\overline{w'w'}$ at Point Alpha was 0.105 $\mathrm{m}^2\mathrm{s}^{-2}$ with values fluctuating considerably more than those in the sub-cloud layer (in agreement with findings from Bretherton et al. (2010), who measured a larger standard deviation in vertical velocity in-cloud vs. sub-cloud). The average in-cloud value of $\overline{w'w'}$ found here is significantly lower than what was found over more remote ocean areas (80°W - 85°W, 20°S) of 0.36 $\mathrm{m}^2\mathrm{s}^{-2}$ (Bretherton et al., 2010). Nocturnal measurements of the Californian Sc deck during DYCOMS-II also revealed a stronger turbulent structure than that measured at Point Alpha, with observations showing in-cloud $\overline{w'w'}$ larger than 0.4 $\mathrm{m}^2\mathrm{s}^{-2}$ with a maximum of 0.5 $\mathrm{m}^2\mathrm{s}^{-2}$ near the base of the Sc deck (Stevens et al., 2005). As discussed in Wood (2012), $\overline{w'w'}$ is typically more vigorous at night due to the buoyancy production being larger from the lack of shortwave radiation absorption, which acts to stabilize the layer. As is found here, Hignett (1991); Nicholls (1984); Ghate et al. (2014) and also

found that $\overline{w'w'}$ peaked in the upper half of the STBL away from any boundaries such as cloud top. Note that the TKE mirrors that of $\overline{w'w'}$ in terms of vertical spatial tendencies.

Considering data collected during aircraft soundings (as opposed to mean values of horizontal flight legs), u-variance, v-variance, w-variance, and the TKE are displayed in Figure 13 Panels (a) through (d), respectively, with the red line representing the mean profile and each gray line representing individual flight profiles. The blue lines represent flight profiles for Nov 1^{st} and Nov 2^{nd}. Panel (e) displays the mean values from each of Panels (a) through (d). The profile of each variable in question shows a near constant value below cloud base, with an increase in-cloud before beginning to decrease near cloud top. Both $\overline{w'w'}$ and TKE reach their peak values at a normalized boundary layer height of $z/z_i = 0.88$ (or a normalized in-cloud location of 0.40). Simulations and observations from Pasquier and Jonas (1998) of in-cloud TKE showed that the maximum TKE occurred in two locations, near cloud top and near cloud base, suggesting that turbulence is being generated through two processes: (1) Cooling at or near cloud top (through evaporation or longwave cooling), resulting in cool, dry downdrafts; (2) Warming near cloud base from the release of latent heat through condensation, resulting in positively buoyant updrafts. However, no conclusions can be made here on whether or not there are two sources of TKE due to the low vertical resolution of the mean values (i.e., averaging over 14 flight profiles). TKE values plummet above the inversion due to the dominance of clear, stable, and subsiding air aloft. The overall maximum in TKE measured (for all 14 flights) is found near a normalized boundary layer height of $z/z_i = 0.60$ (looking at the blue profile line in Figure 13, Panel (d)) during RF11 (Nov 1^{st}). This will be discussed in more detail in Section 4.3.

Looking at individual profiles of TKE, (not shown here), only six of the fourteen flights have a maximum TKE within the cloud layer. Modeling and observations of boundary layer profiles of turbulence from Pasquier and Jonas (1998) showed that mixing and overturning of the boundary layer profile due to buoyancy effects leads to a maximum in turbulence commonly being reached in the sub-cloud layer. Seven of the fourteen flights display two peaks in TKE within the cloud layer, one near cloud base and another near cloud top, signifying evaporative cooling near cloud top and latent heating near cloud base. Of the six flights that have a maximum TKE within the cloud layer, all six display two peaks in the TKE within the cloud layer, one near cloud base and one near cloud top. Having the maximum in TKE in the sub-cloud layer can signify decoupling (Durand and Bourcy, 2001). A slight decoupling can lead to less moisture transport into the Sc layer, resulting in less latent heat release due to condensation. This could be why only one flight has two peaks in TKE within the cloud when the turbulence maximum is reached below cloud, due to latent heat release at cloud base being suppressed.

Figure 14 displays provides the same information format as Figure 13, except for values of buoyancy flux (Panel (a)), latent heat flux LHF (Panel (b)), vertical velocity skewness (Panel (c)), and the cloud droplet number flux (Panel (d)). Note that Figure 14 displays the range of data in the gray envelope, as opposed to showing each individual profile with a single gray line. Both the buoyancy flux and the droplet number concentration flux (from here on $w'N'$) have maximum values at a normalized boundary layer height of $z/z_i = 0.93$ (normalized in-cloud height of 0.59). The peak near cloud middle is due to a combination of the warm/moist updrafts and cool/dry downdrafts meeting, formed by evaporative cooling at cloud top and latent heating near cloud base. The same concept can be extended to $w'N'$, where droplets are activating near cloud base while evaporating near cloud top, suggesting that in the lower cloud the cloud droplet number concentration increases with

updrafts (condensation), while the cloud droplet number concentration decreases with downdrafts (evaporation) in the upper cloud region. According to Pasquier and Jonas (1998), the buoyancy flux should reach a minimum near cloud top from the entrainment of warm, dry air down into the cloud layer. Although the mean profile does not show a decrease at cloud top, the raw data (i.e., unsmoothed) does show a negative buoyancy flux at cloud top. For individual flights, only RF11 (Nov 1^{st}) had a maximum in the buoyancy flux in the sub-cloud layer. The latent heat flux LHF peaks at the surface, but also sees a secondary maximum at a normalized boundary layer height of $z/z_i = 0.99$. The maximum at cloud top can be attributed to the strong q gradient and is due to entrainment of drier air from above the inversion down into the cloud (i.e., also a positive flux since both w' and q' are negative).

Well-mixed STBLs tend to show characteristics of downdrafts that are spatially smaller, but stronger, than updrafts. This results in a negative vertical velocity skewness (from here on $w'w'w'$) through most of the cloud and sub-cloud layer (Nicholls, 1989; Hogan et al., 2009; Ghate et al., 2014). Panel (c) displays that $w'w'w'$ on average is negative throughout the cloud layer and through most of the subcloud layer, having a maximum value near the surface. The minimum values in $w'w'w'$ occurs at cloud base (normalized in-cloud value of 0.04), suggesting that overall, the downdrafts are smallest, yet strongest at cloud base while updrafts are spatially larger, yet weaker.

Figure 15 shows the average buoyancy flux (Panel (a)), LHF latent heat flux (Panel (b)), TKE (Panel (c)), and ϵ (Panel (d)) averaged over all flights for sub below-cloud and for different layers within the cloud. Each black dot represents the average value for individual flights using horizontal leg averages. The blue dots represent mean values using horizontal flight legs, while the red dots represent mean values using flight vertical profile data. Values for in-cloud are calculated for layers between normalized in-cloud height values of 0-0.25 (cloud base), 0.25-0.50 (bottom-middle), 0.50-0.75 (top-middle), and 0.75-1.0 (cloud top). Table 5 summarizes the mean values for each layer. A clear difference in values and trends can be seen between sampling methods. For example, looking at the LHF latent heat flux in Panel (b), we see that the horizontal leg sampling correctly captures the larger LHF latent heat flux at the surface due to evaporation from the ocean surface, whereas the profile samples do not capture this increase at the surface (the profile data is terminated at the start of the 30-m horizontal flight legs, meaning there is limited samples near the surface for the profile method). Conversely, the profile method observed a large increase in TKE at cloud top from evaporative cooling due to entrainment mixing, which is not observed in the horizontal leg method. Another example is the buoyancy flux, which is seen to have a large increase in-cloud as compared to below sub-cloud using the profile method. The horizontal leg method displays a maximum in the top-middle region of the cloud, but the overall buoyancy flux increase in-cloud vs. sub-cloud is compressed as compared to the profile method. In analyzing Table 5, it is clear that the average turbulence (both TKE and ϵ) peaks either in the bottom-middle or top-middle of the cloud (i.e., between a normalized in-cloud height of 0.25-0.75). This is also the two layers in which the buoyancy flux is at a maximum. TKE production near cloud base from latent heat release moves up through the cloud layer, while TKE production near cloud top from evaporative cooling moves down through the cloud layer, resulting in a maximum within the middle of the cloud.

Panels (e) and (f) represent the u, v, and w components of the TKE and ϵ, respectively. The anisotropic conditions present within the turbulent boundary flow can clearly be seen due to the differing values in each component. Although the u and v

components are similar for most layers, differences are evident in the w-component. If the flow was perfectly isotropic, one would expect the same values for each component of the TKE and ϵ.

4.3 RF 11 (November 1st)

Turbulent and boundary layer characteristics have been shown to be abnormal on November 1^{st}, with a minimum in 500-hPa Ggeopotential height, aerosol number concentration, and cloud droplet number concentration. November 1^{st} also had overall mean maximum values of TKE and ϵ, in particular within the sub-cloud layer, along with maximum values in the surface sensible heat flux SHF and drizzle rate. The average drizzle rate in-cloud on November 1^{st} was the largest recorded (a mean in-cloud drizzle water content of 0.025 gm^{-3} measured by the CIP probe) and roughly 4.5 times that of the second largest in-cloud average recorded on November 2^{nd} (0.0055 gm^{-3}), where the average for all other flights was 0.0014 gm^{-3}. A moist layer is present above the boundary layer from looking at profiles of q mixing ratio in Figure 6, leading to the secondary maximum in LWC and cloud thickness (November 2^{nd} had the largest cloud thickness and LWC). Also, visible in Figure 4 is the presence of wind shear near a normalized boundary layer height of $z/z_i = 0.60$.

In order to explore this case further, Figure 16 shows profiles of multiple thermodynamic and turbulent variables as a function of normalized boundary layer height z/z_i. Panel (a) shows profiles of potential temperature θ (blue), liquid water content LWC (black), and mixing ratio q (red). The gray envelope represents the cloud layer, while the orange envelopes represent areas in the sub-cloud layer where the sensible heat flux SHF is negative and TKE and ϵ are enhanced. The potential temperature at the base of the lowest orange envelope begins to deviate from its surface value, decreasing significantly. Normalizing the potential temperature θ from 0 to 1 (where the surface is 0 (the minimum temperature) and the top is 1 (the maximum temperature), we find that the value of the potential temperature θ is 0.32 at cloud top and 0.10 at cloud base, inferring significant entrainment of the warmer, less buoyant air aloft. However, the mixing ratio q within the boundary layer stays relatively constant. This is due to the fact that the entrainment of the warmer air aloft has a larger mixing ratio q than that near the surface of the boundary layer. Significant decoupling is occurring in the sub-cloud layer, near a normalized boundary layer height of $z/z_i = 0.60$ (where the largest TKE and ϵ are located) and 0.40 (secondary maximum in the TKE and ϵ). It is suggested here that precipitation acts to decouple the boundary layer and enhance sub-cloud turbulence due to evaporative cooling of precipitation from the Sc deck above. Zheng et al. (2011) states that the cloud liquid water path reached a maximum on Nov, 1^{st} and Nov 2^{nd} due to the total-water specific humidity above the inversion being larger than that within the boundary layer. The inversion strength became significantly weaker on these two days (as evident from Figure 7) and the boundary layer was decoupled due to drizzle.

Several variables must be considered here. First, the moist layer above the Sc deck can have two effects, including (1) changing the radiative balance at cloud top through increased downwelling longwave radiation (Christensen et al., 2013) and (2) Entrainment of more moist air near cloud top, reducing evaporational cooling (Eastman et al., 2017). Both effects act to reduce cooling (both evaporational and radiational) near cloud top and slows the rate of boundary layer deepening through decreases in entrainment. Eastman and Wood (2018) found that high humidity above the Sc deck acts to slow boundary layer deepening while the entrainment of increased water vapor into the boundary layer results in enhanced cloud cover.

Second, drizzle can have multiple effects on boundary layer structure, including (1) precipitation removes liquid water from the Sc deck, resulting in cloud thinning if the LHF is not large enough to maintain the Sc deck (P.Austin et al., 1995); (2) Warming of the drizzle producing cloud layer occurs through latent heating, acting to stabilize the cloud layer; (3) Changing the stability of the sub-cloud layer depending on the rate of precipitation. Significant proportions of precipitation are known to evaporate before reaching the surface (Comstock et al., 2004; Wood et al., 2015; Zhou et al., 2015). The profile of sub-cloud evaporation determines whether the layer will become more or less unstable. When precipitation is heavier and in the form of large drops it tends to stabilize the boundary layer from evaporational cooling spread over the depth of the sub-cloud layer, with substantial evaporation near the surface stabilizing the boundary layer. When precipitation is lighter and in the form of small drops, cooling persists in the uppermost part of the sub-cloud region, resulting in destabilization of the sub-cloud layer (Feingold et al., 1996; Wood, 2005; Mechem et al., 2012; Rapp, 2016; Ghate and Cadeddu, 2019; Wood, 2012).

As discussed previously, drizzle acts to warm the cloud layer and stabilizes the STBL, which reduces turbulent mixing and induces stratification. However, drizzle also evaporates readily below cloud base, resulting in evaporative cooling and enhanced instability for the subcloud layer (Wood, 2012). Here, precipitation promotes STBL decoupling by reducing the diabatic cooling in the cloud layer through in-cloud latent heating effects resulting in a stabilization of the cloud layer (where the average in-cloud turbulence is the 4^{th} lowest measured on Nov. 1^{st} and lowest measured on Nov. 2^{nd}, see Figure 11). The subcloud evaporation leads to cooling below cloud and a resultant local minimum in the buoyancy flux is created (Bretherton and Wyant, 1997). It is known from Wood (2005) that evaporative cooling shows cooler and more moist characteristics than that of non-precipitating regions. The sensible heat flux (proxy for buoyancy) SHF is observed to be negative from a normalized boundary layer height of $z/z_i \sim 0.4$ up to cloud base, with the minimum and local minimum outlined in the orange envelopes. The LHF is also shown to be slightly enhanced within these regions. This suggests that evaporational cooling is occuring away from the surface, resulting in the largest average turbulence being measured The fact that turbulence peaks in the sub-cloud layer on this day is driven by the instability created from the cool layer below cloud base from precipitation. due to sub-cloud destabilization.

Normally, this process will result in the cloud layer being decoupled form the surface moisture source, leading to a thinning cloud layer. However, the Sc deck is receiving moisture from the upper atmosphere (as seen in the negative latent heat flux LHF above cloud (where w' is negative but q' is positive). This process acts to moisten the boundary layer, which will lower the LCL, and assuming that the boundary layer height z_i does not change, this will thicken the cloud (Randall, 1984). Note that the cloud layer on Nov. 2^{nd} is thicker than that on Nov. 1^{st} by roughly 100 m.

Looking at $w'N'$, an increase occurs near cloud base up to the middle region of the cloud, before decreasing to negative values in the upper half of the cloud. The positive values near cloud base occur due to droplet activation through condensation, while the negative values occur in the upper half of the cloud from upward vertical velocity perturbations having less droplets than that of negative vertical velocity perturbations, suggesting that droplet activation may be occurring near cloud top as well. The vertical velocity skewness $w'w'w'$ also varies between positive and negative values within the sub-cloud layer, providing more evidence that suggesting decoupling is occurring.

To summarize, it appears that the sub-cloud layer is decoupled from the Sc deck due to the evaporative cooling of precipitation. This increases turbulence within the sub-cloud layer, while reducing turbulence in the cloud layer. However, the cloud layer is still supplied with moisture through the entrainment of the more moist air aloft, driving cloud deepening and sustaining the Sc deck. The wind direction shifts from the south in the lower portion of the boundary layer to from the north near a normalized boundary layer height of $z/z_i = 0.60$. Seeing as the The fact that the free atmosphere wind direction extends into the sub-cloud layer, this indicateds that significant entrainment mixing has occurred, resulting in the upper 40% of the boundary layer to share characteristics with the free atmosphere. Note that the maximum value in TKE that is measured on Nov. 1^{st} at a boundary layer height of $z/z_i = 0.60$ (see the blue profile line in Figure 12), matchinges the location at which the wind shear is occurring. However, this spike in TKE cannot be attributed to the wind shear alone, as wind shear that occurs at the inversion for each flight day and within the boundary layer on Nov 4^{th} do not result in large increases in turbulence.

The increase in turbulence seen on Nov 1^{st} is related to latent heating affects and the resulting changes in the buoyancy fluxes. Although not displayed here, profiles for Nov 2^{nd} (the day with the lowest average turbulence) shows a very consistent turbulent profile (no large spikes within or below the cloud layer), suggesting that precipitation has ceased and the boundary layer has been turned over, resulting in little energy remaining for mixing until cooling at cloud top becomes strong enough to support mixing again. It is suggested here that between Nov. 1^{st} and 2^{nd} one of two things occurred, either (1) Precipitation stopped (i.e., the source of instability in the sub-cloud layer) and enhanced turbulent mixing of the sub-cloud layer ceased, (while the cloud layer continued to deepen from the entrainment of more moist air reducing the LCL) or (2) Precipitation continued to occur, leading to evaporation near the surface and a stabilization of the entire boundary layer. Note that although in-cloud drizzle is occurring on Nov. 2^{nd}, there is no evidence of sub-cloud evaporation. Little sources of turbulence can be produced until dryer air moves in and enhanced entrainment cooling near cloud top can resume mixing of the boundary layer, or if precipitation restarts and acts to destabilize the sub-cloud layer.

Comparing RF11 to a well-mixed boundary layer, Figure 17 displays provides the same information format as that of Figure 16, except for RF03 (Oct. 19^{th}). Both potential temperature θ and mixing ratio q appear to be well-mixed throughout the boundary layer, with a slight decrease in the potential temperature θ throughout the cloud layer. TKE, ϵ, the latent heat flux LHF, and the sensible heat flux SHF all have two peaks near cloud base and cloud top, suggesting latent heating near cloud base and evaporative cooling near cloud top. The sensible heat flux SHF also has a negative value above cloud top due to the entrainment of warm, dry air down into the cloud from the stable air above the inversion. The droplet number concentration flux increases near cloud base owing to droplet activation, and sees a sharp decrease near a normalized boundary layer in-cloud height of 0.50, suggesting most of the activation is occurring in the bottom half of the cloud layer. The vertical velocity skewness has a maximum negative value near cloud base, and never has an increase to positive values. The negative TKE flux within the cloud layer suggest that upward moving air is transporting less TKE than that of downward moving air. This negative TKE flux is proposed as evidence of the cloud top entrainment instability (CTEI) process, as proposed in Pasquier and Jonas (1998).

5 Conclusion

Variations in turbulent and meteorological properties within the boundary layer on a flight by flight basis (synoptic variation) have been examined. It has been shown that the influence of a synoptic system on Nov. 1^{st} and Nov. 2^{nd} leads to a deepening of the cloud layer during passage from a moist layer directly above the boundary layer and a A large increase in boundary layer height z_i is observed after passage. Although the pressure is increasing (and subsidence becomes stronger) after the passage of the synoptic system, it is proposed that the moist layer above the boundary layer limits z_i deepening due to reduced evaporational and radiational cooling near cloud top, limiting entrainment. As the synoptic system passes and the upper atmosphere dries, cloud top cooling is enhanced and entrainment acts to deepen z_i, counteracting the fact that subsidence is increasing. TKE Turbulence is shown to be rather weak as compared to other observational studies of Sc decks. TKE is shown to vary around 0.13 m^2s^{-2}, except on the days leading up to and following the synoptic system passage, where the TKE increases rapidly to a maximum on Nov. 1^{st} due to precipitation leading to enhanced turbulence in the sub-cloud layer and then decreases significantly to a minimum on Nov. 2^{nd}. Vertical profiles of turbulent fluxes Analysis over the observation periods indicate:

- As the geopotential height pressure decreases (increases), the boundary layer height and entrainment zone thickness z_i increases (decreases), accompanied by a decrease (increase) of in-cloud and below-cloud in turbulence within the boundary layer. As z_i deepens, cooling near cloud top cannot sustain mixing over the entire depth of the boundary layer, resulting in less turbulence.

- As the LHF and SHF increases (decreases), z_i increases (decreases). When the LHF increases however, the cloud thickness decreases (increases). A larger LHF tends to produce thinner Sc clouds but a larger z_i, suggesting enhanced entrainment which acts to thin the cloud layer while deepening the boundary layer.

- A maximum in TKE on Nov. 1^{st} (both overall average and largest single value measured) is due to precipitation acting to destabilize the subcloud layer (through evaporation away from the surface), while acting to stabilize the cloud layer. This is observed in both the vertical profiles of RF11 and the TKE and ϵ values in Figure 11, where it is shown that the distributions of turbulence for the sub-cloud and cloud layer are completely offset from one another, with the TKE in the sub-cloud layer maximizing for the analysis period, while the TKE in the cloud layer is below the average value for the analysis period. Nov. 2^{nd} has the lowest average turbulence measured (both in-cloud and sub-cloud), and is believed to be a result of (1) lack of cooling near cloud top due to the enhanced moist layer above and (2) Heavy precipitation from the previous day (or sometime prior to the measurements being made) leading to evaporation through the entire sub-cloud layer, stabilizing it.

- Six of the fourteen flights have a maximum TKE within the cloud layer. Seven of the fourteen flights display two peaks in TKE within the cloud layer, one near cloud base and another near cloud top, signifying evaporative cooling near cloud top and latent heating near cloud base. Of the six flights that have a maximum TKE within the cloud layer, all six display two peaks in the TKE within the cloud layer, one near cloud base and one near cloud top. This suggests that enhanced

turbulence below the cloud can act to reduce latent heating and cooling effects within the cloud layer which generate turbulence near cloud bottom and top. Perhaps, enhanced sub-cloud turbulence (as compared to in-cloud) could be an initial indicator that the process of boundary layer decoupling has begun, but has not developed to the point that classical measurement techniques of decoupling (like those discussed in Section 3.3) can measure decoupling yet.

- Analyzing different layers of turbulence over the 14 flights shows that TKE, ϵ, and the buoyancy flux, on average, all reach maximum values near cloud middle (between normalized in-cloud values of 0.25- 0.75).

The results presented here represent a snapshot of data through 14 aircraft flights, with at least a day between any two flights. Therefore, the results presented represent boundary layer conditions that were present at the time of measurement, limiting any analysis of continuously evolving boundary layer and turbulent conditions. For example, being able to analyze the changing thermodynamic and dynamic conditions that resulted in large turbulent changes between Nov 1^{st} and Nov 2^{nd} would be ideal, especially since multiple papers have called for observational studies to assess the impact of drizzle evaporation induced cooling on boundary layer turbulence (Wood et al., 2016; Zheng et al., 2016, 2017). It has also been displayed that how turbulence is analyzed is important to understanding the true extent of how turbulence varies within the boundary layer. Taking large scale averages of turbulent parameters (such as over entire horizontal flight legs) may lead to important smaller resolution variations being averaged out. For example, the vertical profiles presented in Figures 16 and 17 show much more detail in the vertical trends as compared to the averaged results of horizontal leg means displayed in Figure 12. Future work will involve using the turbulent analysis presented here to better understand the interactions between droplet clustering (or preferential concentration) and turbulence within Sc clouds, including variables that may influence the components just mentioned, such as aerosol number concentration, cloud height, and precipitating vs. non-precipitating regions of cloud.

Data availability. All cabin data from different aircraft platforms can be found on the VOCALS-Rex website at https://archive.eol.ucar.edu/projects/vocals/rex.html (last access: 02 February 2020). All NCEP/NCAR reanalysis data can be found from NOAA at https://www.esrl.noaa.gov/psd/data/gridded/data.ncep.reanalysis.html.

Author contributions. DSD and JDSG contributed equally to both the analysis and the writing of this paper.

Competing interests. There are no competing interests to declare

Acknowledgements. We thank the CIRPAS Twin Otter crew and personnel, including pilots Mike Hubble and Chris McGuire, for their effort and support during the field program, along with any individual who contributed to the planning and execution of VOCALS-Rex. This work was funded by NASA NESSF grant 80NSSC18K1406.

References

Ackerman, A. S., van Zanten, M. C., Stevens, B., Savic-Jovcic, V., and Bretherton, C. S.: Large-eddy simulations of a drizzling, stratocumulus-topped marine boundary layer, Mon. Weather Rev., 137, 1083–1110, 2009.

Akinlabi, E. O., Waclawczyk, M., Mellado, J. P., and Malinowski, S. P.: Estimating Turbulence Kinetic Energy Dissipation Rates in the Numerically Simulated Stratocumulus Cloud-Top Mixing Layer: Evaluation of Different Methods, J. Atmos. Sci., 76, 1471–1488, 2019.

Albrecht, B., Randall, D. A., and Nicholls, S.: Observations of marine stratocumulus during FIRE, Bull. Amer. Meteor. Soc., 69, 619–626, 1988.

Albrecht, B. A., Penc, R. S., and Schubert, W. H.: An observational study of cloud-topped mixed layers, J. Atmos. Sci., 42, 800–822, 1985.

Albrecht, B. A., Jensen, M. P., and Syrett, W. J.: Marine boundary layer structure and fractional cloudiness, J. Geophys. Res., 100, 14 209–14 222, 1995.

Barret, B. S., Garreaud, R. D., and Falvey, M.: Effect of the Andes cordillera on precipitation from a midlatitude cold front, Mon. Weather Rev., 137, 3092–3109, 2009.

Blot, R., Clarke, A. D., Freitag, S., Kapustin, V., Howell, S. G., Jensen, J. B., Shank, L. M., McNaughton, C. S., and Brekhovskikh, V.: Ultrafine sea spray aerosol over the southeastern Pacific: open-ocean contributions to marine boundary layer CCN, Atmos. Chem. Phys., 13, 7263–7278, 2013.

Bretherton, C. S. and Wyant, M. C.: Moisture transport, lower-tropospheric stability, and decoupling of cloud-topped boundary layers, J. Atmos. Sci., 54, 148–167, 1997.

Bretherton, C. S., Uttal, T., Fairall, C. W., Yuter, S. E., Weller, R. A., Baumgardner, D., Comstock, K., Wood, R., and Raga, G. B.: The Epic 2001 Stratocumulus Study, B. Am. Meteorol. Soc., 85, 967–977, 2004.

Bretherton, C. S., Uchida, J., and Blossey, P.: Slow manifolds and multiple equilibria in stratocumulus-capped boundary layers, J. Adv. Model. Earth Syst., 2, https://doi.org/10.3894/JAMES.2010.2.14., 2010.

Caughey, S. J., Crease, B. A., and Roach, W. T.: A field-study of nocturnal stratocumulus. 2. Turbulence structure and entrainment, Quart. J. Roy. Meteor. Soc., 108, 125–144, 1982.

Chamecki, M. and Dias, N. L.: The local isotropy hypothesis and the turbulent kinetic energy dissipation rate in the atmospheric surface layer, Q. J. Roy. Meteor. Soc., 130, 2377–2752, 2004.

Chapman, D. and Browning, K. A.: Measurements of dissipation rate in frontal zones, Quart. J. Roy. Meteor. Soc., 127, 1939–1959, 2001.

Christensen, M. W., Carrio, G. G., Stephens, G. L., and Cotton, W. R.: Radiative impacts of free-troposphere clouds on the properties of marine stratocumulus, J. Atmos. Sci., 70, 3102–3118, 2013.

Comstock, K., Yuter, S., and Wood, R.: Reflectivity and rain rate in and below drizzling stratocumulus, Quart. J. Roy. Meteor. Soc., 130, 2891–2919, 2004.

de Roode, S. R. and Duynkerke, P. G.: Dynamics of cumulus rising into stratocumulus as observed during the first 'Lagrangian' experiment of ASTEX, Quart. J. Roy. Meteor. Soc., 122, 1597–1623, 1996.

Devenish, B. J., Bartello, P., Brenguier, J.-L., Collins, L. R., Grabowski, W. W., Ijzermans, R. H. A., Malinowski, S. P., Reeks, M. W., Vassilicos, J. C., Wang, L.-P., and Warhaft, Z.: Droplet growth in warm turbulent clouds, Q. J. Roy. Meteorol. Soc., 138, 1401–1429, 2012.

Durand, P. and Bourcy, T.: Observations of the turbulence structure wihtin two stratocumulus-topped, marine boundary layers, Boundary Layer Meteorology, 99, 105–125, 2001.

Eastman, R. and Wood, R.: The competing effects of stability and humidity on Subtropical Stratocumulus Entrainment and Cloud Evolution from a Lagrangian Perspective, J. Atmos. Sci, 75, 2563–2578, 2018.

Eastman, R., Wood, R., and O, K. T.: The subtropical stratocumulus-topped planetary boundary layer: A climatology and the Lagrangian evolution, J. Atmos. Sci., 74, 2633–2656, 2017.

Engeln, A. V. and Teixeira, J.: A planeltary boundary layer height climatology derived from ECMWF Reanalysis Data, J. Climate, 26, 6575–6590, 2013.

Feingold, G., Stevens, B., Cotton, W. R., and Frisch, A. S.: The relationship between drop in-cloud residence time and drizzle production in numerically simulated stratocumulus clouds, J. Atmos. Sci., 53, 1108–1112, 1996.

Frank, H. P.: Boundary layer structure in two fronts passing a tower, Meteor. Atmos. Phys., 53, 95–109, 1994.

Frisch, U.: Turbulence–The Legacy of A. N. Kolmogorov, Cambridge University Press, 1995.

Galewsky, J.: Using stable isotops in water vapor to diagnose relationships between lower-tropospheric stability, mixing, and low-cloud cover near the island of Hawaii, Gephys. Res. Lett., 45, 297–305, 2018.

Garreaud, R. D. and Rutllant, J.: Coastal Lows along the Subtropical West Coast of South America: Numerical Simulation of a Typical Case, Mon.Weather Rev., 131, 891–908, 2003.

Gesso, S. D., van der Dussen, J. J., Siebesma, A. P., de Roode, S. R., and Boutle, I. A.: A single-column model intercomparison on the stratocumulus representation in present-day and future climate, J. Adv. Model. Earth Syst., 7, 617–647, 2015.

Ghate, V. P. and Cadeddu, M. P.: Drizzle and Turbulence Below Closed Cellular Marine Stratocumulus Clouds, J. Geophys. Res. Atmos, 124, 5724–5737, 2019.

Ghate, V. P., Albrecht, B. A., Miller, M. A., Brewer, A., and Fairall, C. W.: Turbulence and Radiation in Stratocumulus-Topped Marine Boundary Layers: A Case Study from VOCALS-REx, J. Appl. Meteor. Climatol., 53, 117–135, 2014.

Heinze, R., Mironov, D., and Raasch, S.: Second-moment budgets in cloud topped boundary layers: A large-eddy simulation study, J. Adv. Model. Earth Syst., 7, 510–536, 2015.

Hersbach, H., Bell, B., Berrisford, P., and et. al.: The ERA5 global reanalysis, Q. J. R. Meteorol. Soc., p. 1:51, 2020.

Hignett, P.: Observations of diurnal variation in a cloud-capped marine boundary layer, J. Atmos. Sci., 48, 1471–1482, 1991.

Hogan, R. J., Grant, L., Illingworth, A. J., Pearson, G. N., and O'connor, E. J.: Vertical velocity variance and skewness in clear and cloud-topped boundary layers as revealed by Doppler Lidar, Quart. J. Roy. Meteor. Soc., 135, 635–643, 2009.

Jen-La Plante, I., Ma, Y., Nurowska, K., Gerber, H., Khelif, D., Karpinska, K., Kopec, M. K., Kumala, W., and Malinowski, S. P.: Physics of Stratocumulus Top (POST): turbulence characteristics, Atmos. Chem. Phys., 16, 9711–9725, 2016.

Jia, H., Ma, X., and Liu, Y.: Exploring aerosol–cloud interaction using VOCALS-REx aircraft measurements, Atmos. Chem. Phys., 19, 7955–7971, 2019.

Jones, C. R., Bretherton, C. S., and Leon, D.: Coupled vs. Decoupled boundary layers in VOCALS-REx, Atmos. Chem. Phys., 11, 7143–7153, 2011.

Kistler, R., Kalnay, E., Collins, W., Saha, S., White, G., Woollen, J., Chelliah, M., Ebisuzaki, W., Kanamitsu, M., Kousky, V., can den Dool, H., Jeene, R., and Fiorino, M.: The NCEP-NCAR 50-Year Reanalysis: Monthly Means CD-ROM and Documentation, B. Am. Meteorol. Soc., 82, 247–267, 2001.

Kolmogorov, A. N.: The local structure of turbulence in incompressible viscous fluid for very large Reynolds numbers, Dokl. Akad. Nauk SSSR, 30, 301–304, 1941.

Kopec, M. K., Malinowski, S. P., and Piotrowski, Z. P.: Effects of wind shear and radiative cooling on the stratocumulus- topped boundary layer, Quart. J. Roy. Meteor. Soc., 142, 3222–3233, 2016.

Kurowski, M. J., Malinowski, S. P., and Grabowski, W.: A numerical investigation of entrainment and transport within a stratocumulus-topped boundary layer, Q. J. R. Meteorol. Soc., 135, 77–92, 2009.

Lenschow, D. H., Mann, J., and Kristensen, L.: How long is long enough when measuring fluxes and other turbulence statistics?, J. Atmos. Oceanic Technol, 11, 661–673, 1994.

Lenschow, D. H., Wulfmeyer, V., and Senff, C.: Measuring second-through fourth-order moments in noisy data, J. Atmos. Oceanic Technol., 17, 1330–1347, 2000.

Lewellen, D. C., Lewellen, W. S., and Yoh, S.: Influence of Bowen ratio on boundary layer cloud structure, J. Atmos. Sci., 53, 175–187, 1996.

Lilly, D. K.: Models of cloud-topped mixed layers under a strong inversion, Quart. J. Roy. Meteor. Soc., 94, 292–309, 1968.

Malinowski, S. P., Gerber, H., Plante, I. J.-L., Kopec, M. K., Kumala, W., Nurowska, K., Chuang, P. Y., Khelif, D., and Haman, K. E.: Physics of Stratocumulus Top (POST): Turbulent mixing across capping inversion, Atmos. Chem. Phys., 13, 12 171–12 186, 2013.

McNicholas, C. and Turner, D. D.: Characterizing the convective boundary layer turbulence with a High Spectral Resolution Lidar, J. Geophys. Res. Atmos, 119, 12,910–12,927, 2014.

Mechem, D., Yuter, S. E., and DeSzoeke, S. P.: Thermodynamic and Aerosol Controls in Southeast Pacific Stratocumulus, J. Atmos. Sci., 69, 1250–1266, 2012.

Mellado, J. P.: Cloud-Top Entrainment in Stratocumulus Clouds, Annu. Rev. Fluid Mech., 49, 149–169, 2017.

Mellado, J. P., Stevens, B., Schmidt, H., and Peters, N.: Two-fluid formulation of the cloud-top mixing layer for direct numerical simulation, Theor. Comput. Fluid Dyn., 24, 511–536, 2014.

Moeng, C. H., Shen, S. H., and Randall, D. A.: Physical processes within the nocturnal stratus-topped boundary layer, J. Atmos. Sci., 49, 2384–2401, 1992.

Nicholls, S.: The dynamics of stratocumulus: Aircraft obser- vations and comparisons with a mixed layer model, Quart. J. Roy. Meteor. Soc., 110, 783–820, 1984.

Nicholls, S.: The structure of radiatively driven convection in stratocumulus, Quart. J. Roy. Meteor. Soc., 115, 487–511, 1989.

Nicholls, S. and Leighton, J.: An observational study of the structure of stratiform cloud sheets: Part I. Structure, Quart. J. Roy. Meteor. Soc., 112, 431–460, 1986.

Noda, A. T. and Satoh, M.: Intermodel variances of subtropical stratocumulus environments simulated in CMIP5 models., Geophys. Res. Lett., 41, 7754–7761, 2014.

Painemal, D. and Zuidema, P.: The first aerosol indirect effect quantified through airborne remote sensing during VOCALS-REx, Atmos. Chem. Phys., 13, 917–931, 2013.

Palm, S. P., Schwemmer, G. K., Vandemark, D., Evans, K. D., and Miller, D. O.: The estimation of surface latent heat flux over the ocean and its relationship to Marine Atmospheric Boundary Layer (MABL) structure, Proc. SPIE, https://doi.org/10.1117/12.366432, 1999.

Pasquier, J. R. M. and Jonas, P. R.: Turbulent transport in fields of warm cumulus clouds, Quart. J. Met. Soc., 124, 363–387, 1998.

P.Austin, Wang, Y., Pincus, R., and Kujala, V.: Precipitation in stratocumulus clouds: Observations and modeling results, J. Atmos. Sci., 52, 2329–2352, 1995.

Petters, J. L., Jiang, H., Feingold, G., Rossiter, D. L., Khelif, D., Sloan, L. C., and Chuang, P. Y.: A comparative study of the response of modeled non-drizzling stratocumulus to meteorological and aerosol perturbations, Atmos. Chem. Phys., 13, 2507–2529, 2013.

Pinsky, M. B. and Khain, A. P.: Simulations of drop fall in a homogeneous isotropic turbulent flow, Atmos. Res., 40, 223–259, 1996.

Poggi, D. and Katul, G. G.: Two-dimensional scalar spectra in the deeper layers of a dense and uniform model canopy, Bound. Layer Meteor., 121, 267–281, 2006.

Rahn, D. A. and Garreaud, R.: Marine boundary layer over the subtropical southeast Pacific during VOCALS-REx – Part 2: Synoptic variability, Atmos. Chem. Phys., 10, 4507–4519, 2010a.

Rahn, D. A. and Garreaud, R.: Marine boundary layer over the subtropical southeast Pacific during VOCALS-REx – Part 1: Mean structure and diurnal cycle, Atmos. Chem. Phys., 10, 4491–4506, 2010b.

Randall, D. A.: Stratocumulus cloud deepening through entrainment, Tellus, 36A, 446–457, 1984.

Randall, D. A., Coakley, J. A., Fairall, C. W., Knopfli, R. A., and Lenschow, D. H.: Outlook for research on marine subtropical stratocumulus clouds, Bull. Amer. Meteor. Soc., 64, 1290–1301, 1984.

Rapp, A. D.: Observational evidence linking precipitation and mesoscale cloud fraction in the southeast Pacific, Geophy. Res. Lett., 43, 7267–7273, 2016.

Rutllant, J. A., Munoz, R. C., and Garreaud, R. D.: Meteorological observations on the northern Chilean coast during VOCALS-REx, Atmos. Chem. Phys., 13, 3409–3422, 2013.

Schubert, W. H., Wakefield, J. S., Steiner, E. J., and Cox, S. K.: Marine stratocumulus convection. Part I: Governing equations and horizontally homogeneous solutions, J. Atmos. Sci., 36, 1286–1307, 1979.

Schulz, B. and Mellado, J. P.: Wind Shear Effects on Radiatively and Evaporatively Driven Stratocumulus Tops, J. Atmos. Sci., 75, 3245–3268, 2018.

Shapiro, M. A., Hampel, T., Rotzoll, D., and Mosher, F.: The frontal hydraulic head: A microscale (1 km) triggering mechanism for mesoconvective weather systems, Mon. Wea. Rev., 113, 1166–1183, 1985.

Shaw, R. A.: Particle–Turbulence Interactions in Atmospheric Clouds, Annu. Rev. Fluid Mech., 35, 183–227, 2003.

Siebert, H., Lehmann, K., and Wendisch, M.: Observations of small-scale turbulence and energy dissipation rates in the cloudy boundary layer, J. Atmos. Sci., 63, 1451–1466, 2006.

Stevens, B., Moeng, C.-H., Ackerman, A. S., Bretherton, C. S., Chlond, A., de Roode, S., Edwards, J., Golaz, J.-C., Jiang, H., Khairoutdinov, M., Kirkpatrick, M. P., Lewellen, D. C., Lock, A., Muller, F., Stevens, D. E., Whelan, E., and Zhu, P.: Evaluation of large-eddy simulations via observations of nocturnal marine stratocumulus, Mon. Wea. Rev., 133, 1443–1462, 2005.

Taylor, P. A., Salmon, J. R., and Stewart, R. E.: Mesoscale observations of surface fronts and low pressure centres in Canadian East Coast storms, Bound. Layer Meteor., 64, 15–54, 1993.

Terai, C. R., Wood, R., Leon, D. C., and Zuidema, P.: Does precipitation susceptibility vary with increasing cloud thickness in marine stratocumulus?, Atmos. Chem. Phys., 12, 4567–4583, 2013.

Toniazzo, T., Abel, S. J., Wood, R., Mechoso, C. R., Allen, G., and Shaffrey, L. C.: Large-scale and synoptic meteorology in the south-east Pacific during the observations campaign VOCALS-REx in austral Spring 2008, Atmos. Chem. Phys., 11, 4977–5009, 2011.

Turner, D. D., Wulfmeyer, V., and Scarino, A. J.: Aircraft evaluation of ground-based Raman lidar water vapor turbulence profiles in convective mixed layers, J. Atmos. Oceanic Technol., 31, 1078–1088, 2014.

Twohy, C. H., Anderson, J. R., Toohey, D. W., Andrejczuk, M., Adams, A., Lytle, M., George, R. C., Wood, R., Saide, P., Spak, S., Zuidema, P., and Leon, D.: Impacts of aerosol particles on the microphysical and radiative properties of stratocumulus clouds over the southeast Pacific Ocean, Atmos. Chem. Phys., 13, 2541–2562, 2013.

Wood, R.: Drizzle in stratiform boundary layer clouds. Part I: Vertical and horizontal structure, J. Atmos. Sci., 62, 3011–3033, 2005.

Wood, R.: Stratocumulus Review, Mon. Weather Rev., 140, 2373–2423, 2012.

Wood, R. and Bretherton, C. S.: Boundary Layer Depth, Entrainment, and Decoupling in the Cloud-Capped Subtropical and Tropical Marine Boundary Layer, J. Climate, 17, 3576–3588, 2004.

Wood, R. and Hartmann, D. L.: Spatial variability of liquid water path in marine boundary layer clouds: The importance of me- soscale cellular convection, J. Climate, 19, 1748–1764, 2006.

Wood, R., Mechoso, C. R., Bretherton, C. S., Weller, R. A., Huebert, B., Straneo, F., Albrecht, B. A., Coe, H., Allen, G., Vaughan, G., Duam, P., Fairall, C., CHand, D., Klenner, L. G., Garreaud, R., Grados, C., Covert, D. S., Bates, T. S., Krejci, R., Russell, L. M., de Szoeke, S., Brewer, A., Yuter, S. E., Springston, S. R., Chaigneau, A., Toniazzo, T., Minnis, P., Palikonda, R., Abel, S. J., Brown, W. O. J., Williams, S., Fochesatto, J., Brioude, J., and Bower, K. N.: The VAMOS Ocean-CLoud-Atmosphere-Land Study Regional Experiment (VOCALS-Rex): goals, platforms, and field operations, Atmos. Chem. Phys., 11, 627–654, 2011.

Wood, R., Wyant, M., Bretherton, C. S., Remillard, J., Kollias, P., and Fletcher, J.: Clouds, aerosols, and precipitation in the marine boundary layer: An ARM mobile facility deployment, Bull. Amer. Meteor. Soc., 96, 419–440, 2015.

Wood, R., Jensen, M. P., Wang, J., Bretherton, C. S., Burrows, S. M., Genio, A. D. D., and et al.: Planning the next decade of coordinated research to better understand and simulate marine low clouds, Bull. Amer. Meteor. Soc., 79, 1699–1702, 2016.

Wulfmeyer, V.: Investigation of turbulent processes in the lower troposphere with water vapor DIAL and radar RASS, J. Atmos. Sci., 56, 1055–1076, 1999.

Wulfmeyer, V., Pal, S., Turner, D. D., and Wagner, E.: Can water vapour Raman lidar resolve profiles of turbulent variables in the convective boundary layer?, Bound.-Layer Meteor., 136, 253–284, 2010.

Wulfmeyer, V., Muppa, S. K., Behrendt, A., Hammann, E., Spath, F., Sorbjan, Z., Turner, D. D., and Hardesty, R. H.: Determination of Convective Boundary Layer Entrainment Fluxes, Dissipation Rates, and the Molecular Destruction of Variances: Theoretical Description and a Strategy for Its Confirmation with a Novel Lidar System Synergy, J. Atmos. Sci., 73, 667–692, 2016.

Wyant, M. C., Wood, R., Bretherton, C. S., Mechoso, C. R., Bacmeister, J., Balmaseda, M. A., Barrett, B., Codron, F., Earnshaw, P., Fast, J., Hannay, C., Kaiser, J. W., Kitagawa, H., Klein, S. A., Kohler, M., Manganello, J., Pan, H. L., Sun, F., Wang, S., and Wang, Y.: The PreVOCA experiment: modeling the lower troposphere in the Southeast Pacific, Atmos. Chem. Phys., 10, 4757–4774, 2010.

Young, G. S. and Johnson, R. H.: Meso and microscale features of a Colorado cold front, J. Climate Appl. Meteor., 23, 1315–1325, 1984.

Zhang, M., Bretherton, C. S., Blossey, P. N., Austin, P. H., Bacmeister, J. T., and et al.: CGILS: results from the first phase of an international project to understand the physical mechanisms of low cloud feedbacks in single column models, J. Adv. Model. Earth Syst., 5, 826–842, 2013.

Zheng, X., Albrecht, B. A., Minnis, P., Ayers, K., and Jonson, H. H.: Observed aerosol and liquid water path relationships in marine stratocumulus, Geophys. Res. Lett., 37, L17 803, 2010.

Zheng, X., Albrecht, B., Jonsson, H. H., Khelif, D., Feingold, G., Minnis, P., Ayers, K., Chuang, P., Donaher, S., Rossiter, D., Ghate, V., Ruiz-Plancarte, J., and Sun-Mack, S.: Observations of the boundary layer, cloud, and aerosol variability in the southeast Pacific near-coastal marine stratocumulus during VOCALS-REx, Atmos. Chem. Phys., 11, 9943–9952, 2011.

Zheng, X., Klein, S. A., Ma, H. Y., Bogenschutz, P., Gettelman, A., and Larson, V. E.: Assessment of marine boundary layer cloud simulations in the CAM with CLUBB and updated microphysics scheme based on ARM observations from the Azores, J. Geophys. Res. Atmos, 121, 8472–8492, 2016.

Zheng, X., Klein, S. A., Ma, H.-Y., Caldwell, P., Larson, V. E., Gettelman, A., and Bogenschutz, P.: A cloudy planetary boundary layer oscillation arising from the coupling of turbulence with precipitation in climate simulations, J. Adv. Model.Earth Syst, 9, 1973–1993, 2017.

Zhou, X., Kollias, P., and Lewis, E. R.: Clouds, precipitation, and marine boundary layer structure during the MAGIC field campaign, J. Climate, 28, 2420–2442, 2015.

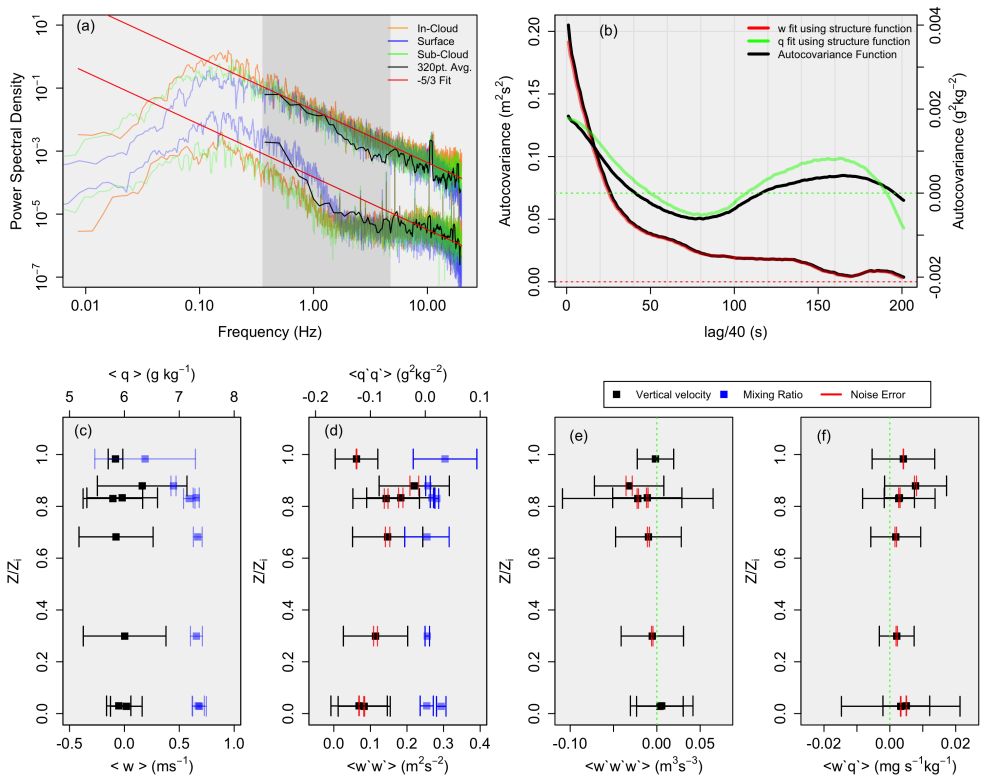

Figure 1. All data presented is from RF3. Panel (a): Power spectral density for three different horizontal flight legs, including in-cloud (orange), sub-cloud (green), and near surface (blue) fit with a -5/3 power law (red), where the upper fit is vertical velocity (m^2s^{-1}), and the lower fit is q (g^2kg^{-2}). The black specra overlaid represents a single specra using a 320-point average. The light gray envelope represents the 0.3 to 5-Hz range; Panel (b): Autocovariacne functions of vertical velocity and q (black) with the fit structure function (green for q and red for vertical velocity); Panel (c): leg mean vertical velocity (black) and q (blue), where the error bars represent the square root of the total variance; Panel (d): As in Panel (c), except for the variance. Note that red error bars represent the noise error, while the remaining error bars represent the sampling error; Panel (e): As in Panel (d), except for vertical velocity skewness; Panel (f); As in Panel (d), except for the flux $w^{'}q^{'}$.

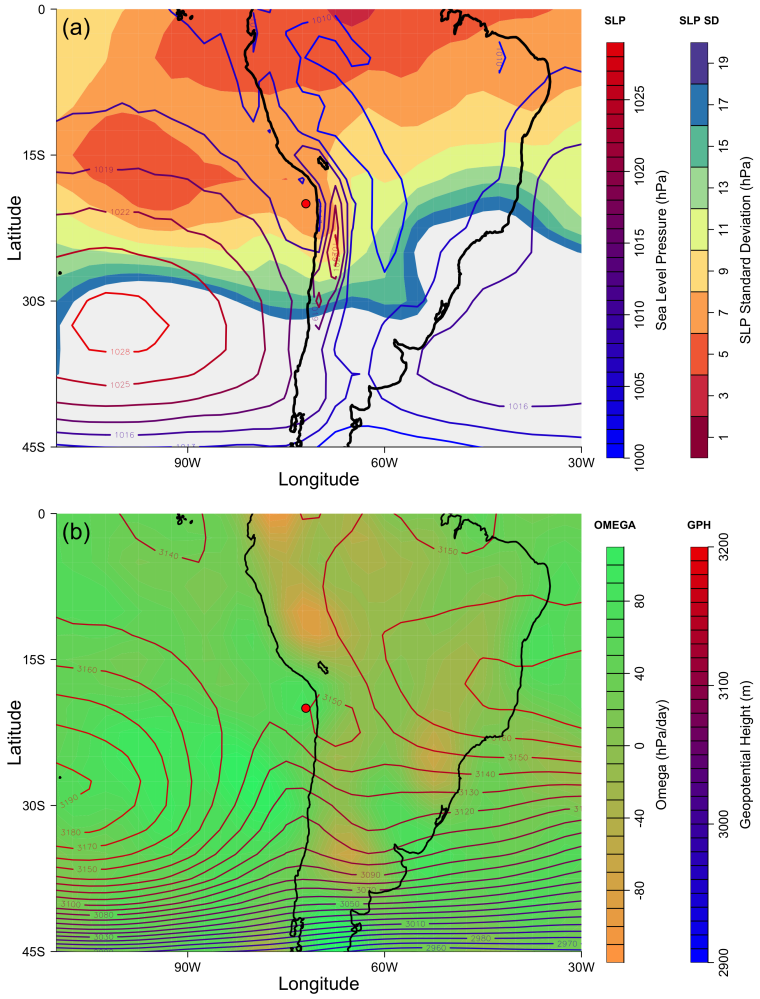

Figure 2. Panel (a): Mean sea level pressure (hPa) between October 19^{th} and November 12^{th} with the standard deviation overlaid. Note that the contours are every 3-hPa; Panel(b): Mean 700-hPa geopotential height with mean omega overlaid at the same level. Contours are every 10-m. The red dot in both panels represents the location of Point Alpha.

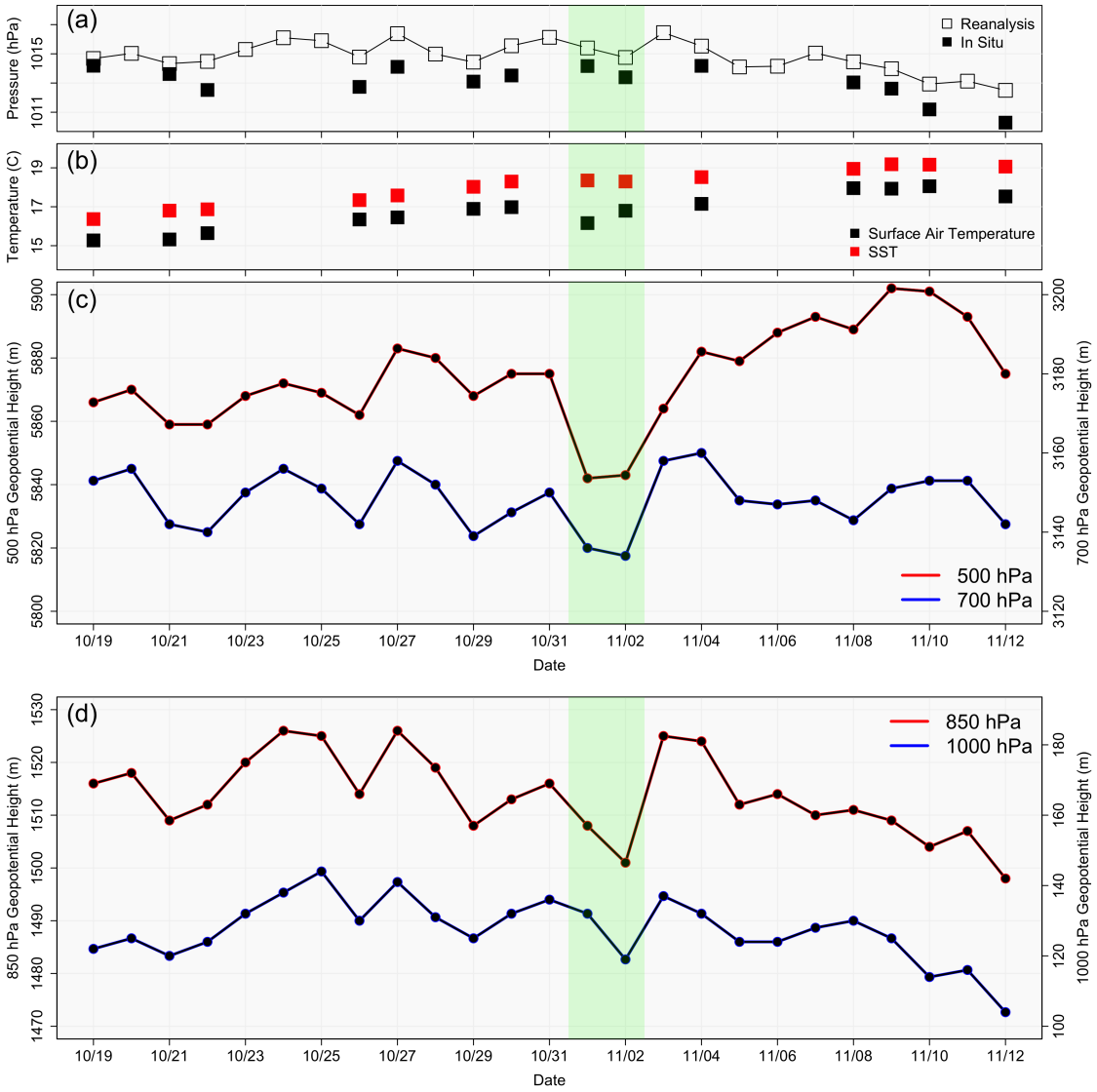

Figure 3. Panel (a): NCEP/NCAR reanalysis (open squares) and flight data (solid squares); Panel (b): Sea surface temperature and atmospheric surface temperature collected from flight data; Panel (c): 500-hPa (red) and 700-hPa (blue) geopotential height data from NCEP/NCAR reanalysis data; Panel (d): Same as panel (c), except for 850-hPa (red) and 1000-hPa (blue).

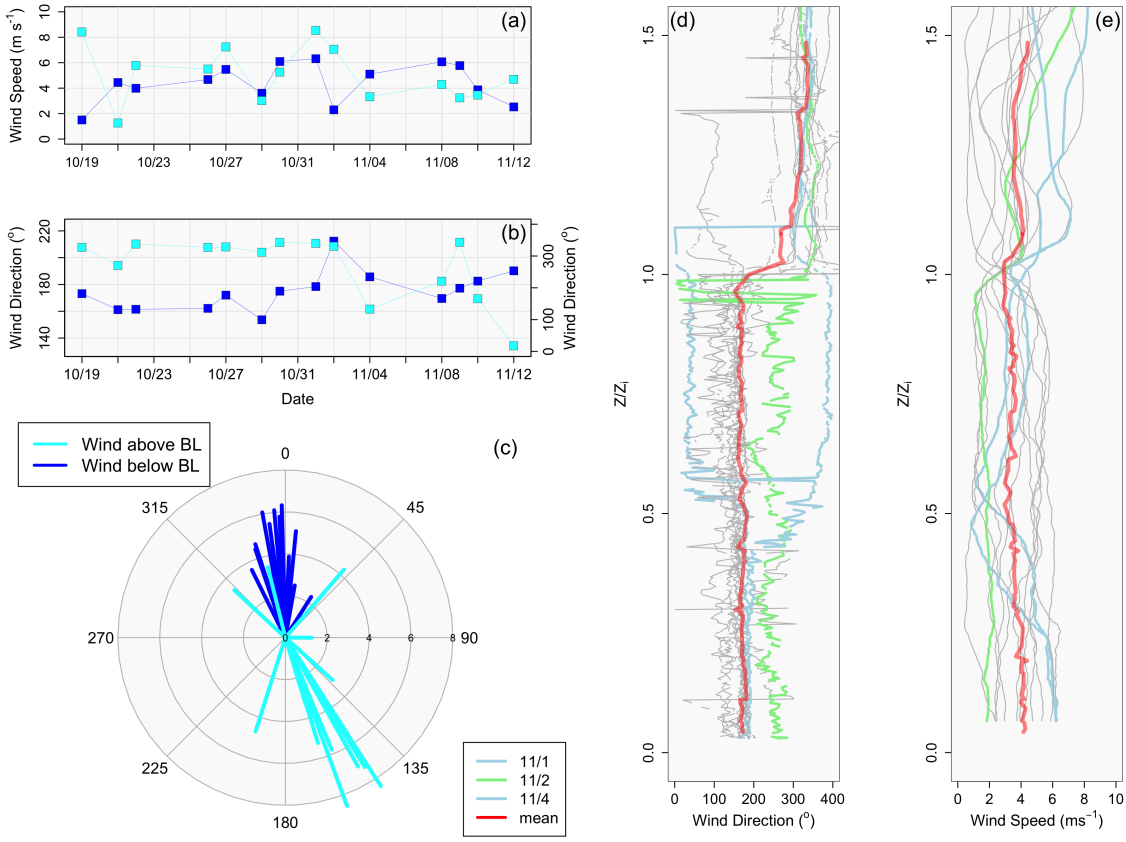

Figure 4. Panel(a): Wind speed (ms^{-1}) at the surface collected during 30-m horizontal flight legs (dark blue) and above the inversion collected during horizontal flight legs above the boundary layer (light blue); Panel (b): Same as panel (a), except for wind direction (degree); Panel (c): Vectors showing wind direction from panel (b); Panel (d): Vertical profiles (collected during aircraft soundings) of wind direction for each flight day plotted vs. normalized boundary layer height. November 1^{st} and 4^{th} are displayed in light blue, November 2^{nd} is green, and the mean wind direction is represented by red.

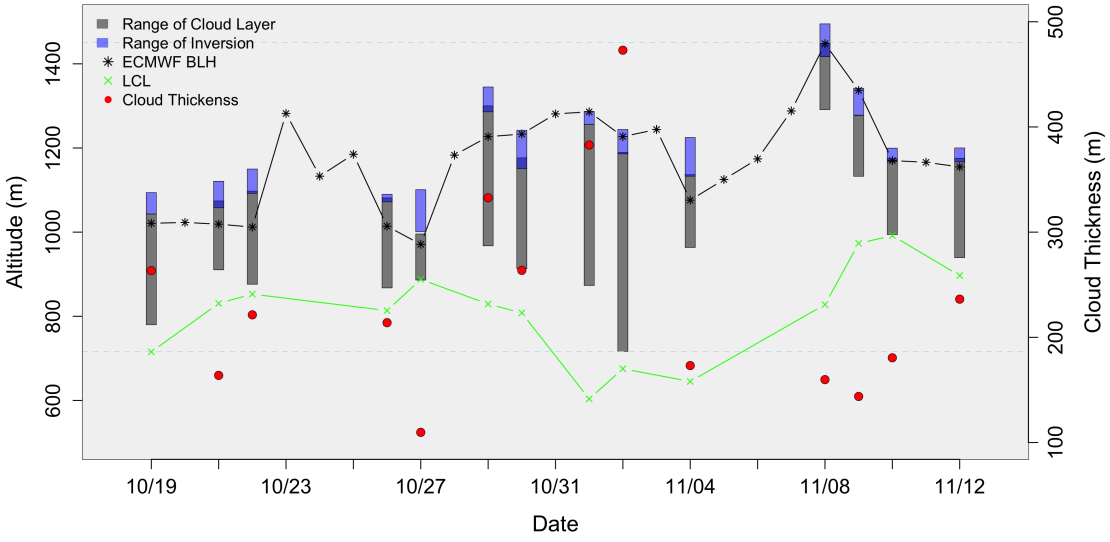

Figure 5. Shows the range of the cloud (gray) and inversion (blue) layer as a function of altitude for each RF. The top of each gray profile represents cloud top and boundary layer top z_i. The bottom of each gray profile represents cloud base. Cloud thickness (represented as a single value) is represented by each red dot (right y-axis). The LWC and ECMWF-z_i are provided with the black star and green x, repsectively.

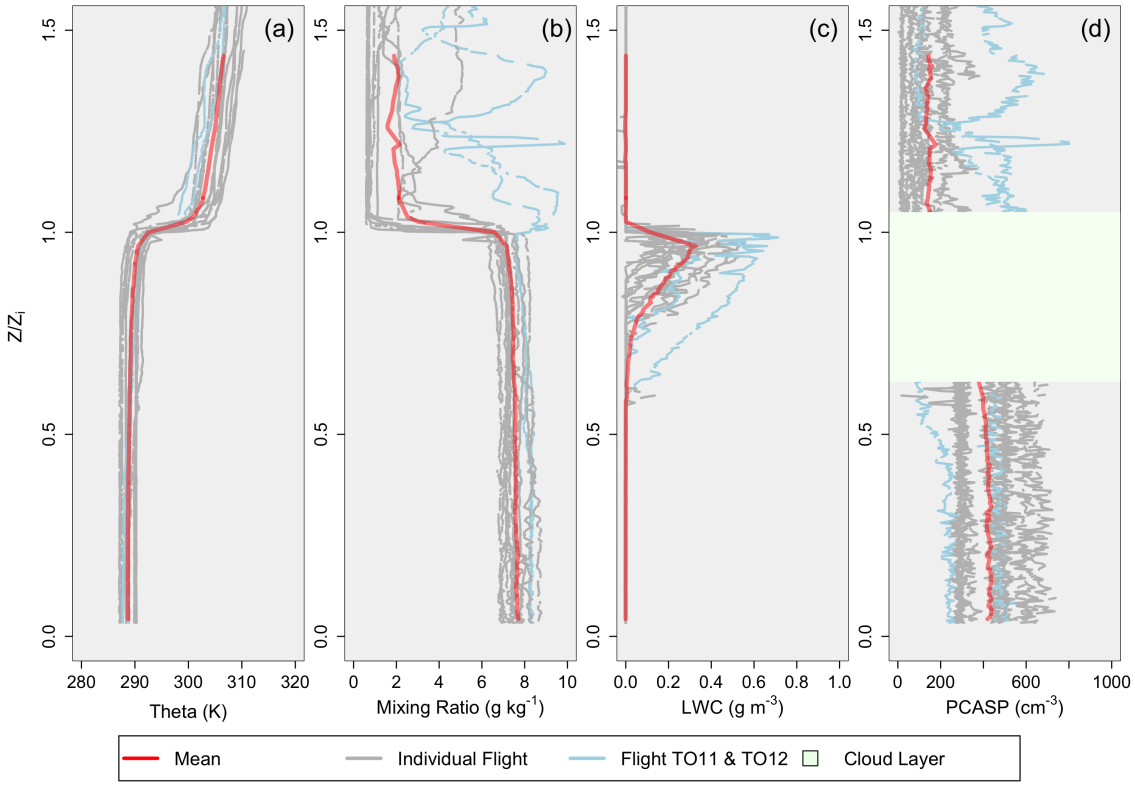

Figure 6. Profiles scaled by the boundary layer heights. (a) potential temperature (K); (b) mixing ratio (g kg^{-1}); (c) liquid water content (g m^{-3}); (d) Aerosol number concentration (cm^{-3}). The red profile represents the mean value, and the two blue profiles represent RF 11 and RF 12. The green layer represents the relative cloud layer for panel (d), as aerosol data cannot be collected in the cloud layer.

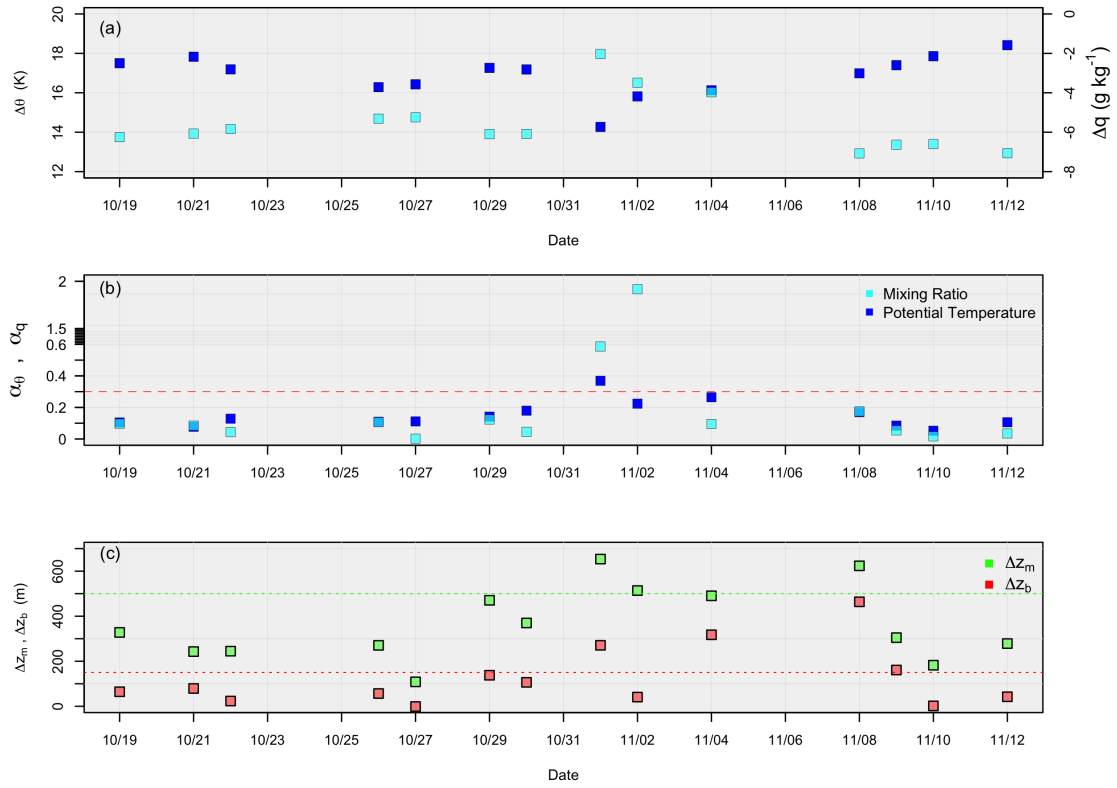

Figure 7. (a) The decoupling parameters; (b) potential temperature (left y-axis) and mixing ratio (right y-axis) differences across the inversion, for all 14 flights; (b)The decoupling parameters for mixing ratio (light blue) and potential temperature (dark blue), where the red dashed line represents the 0.30 value; (c) Mixed layer cloud thickness (green) and the difference between cloud base and the LCL (red), where the red dashed line represents the 500 value and the green dashed line represents the 150 value.

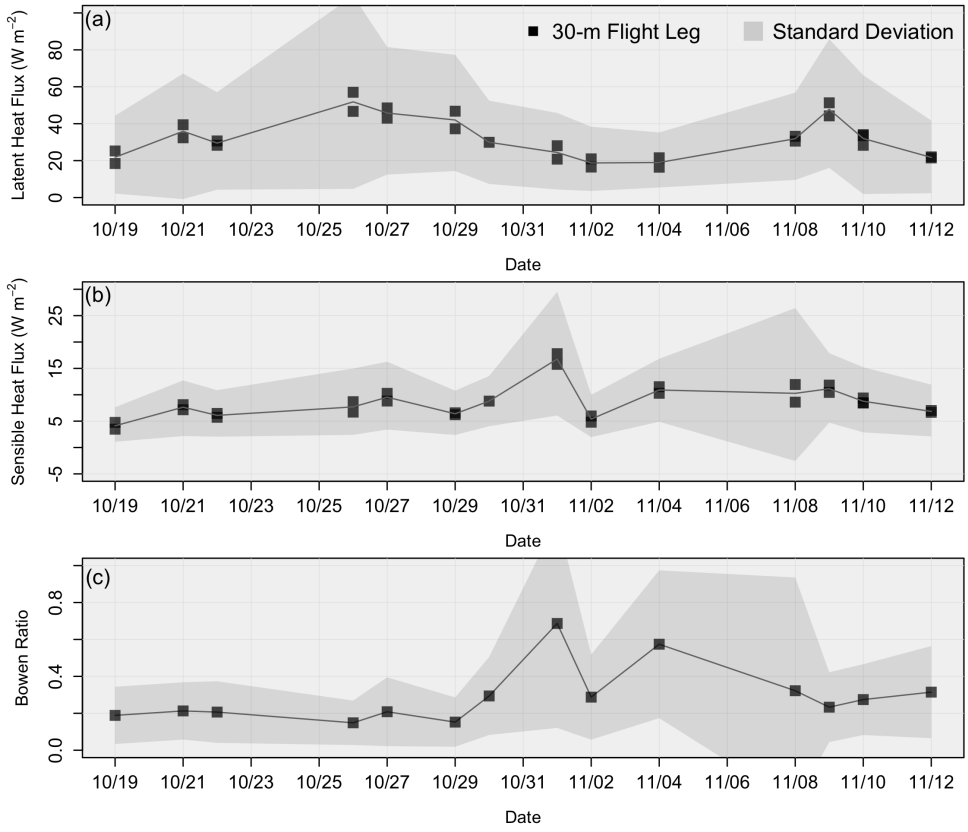

Figure 8. Values of (a) surface latent heat flux (Wm^{-2}); (b) Sensible heat flux (Wm^{-2}); and (c) the Bowen ratio, for each flight day. Note that each black square is a mean of a 30-m horizontal flight leg, while the gray envelope represents the standard deviation.

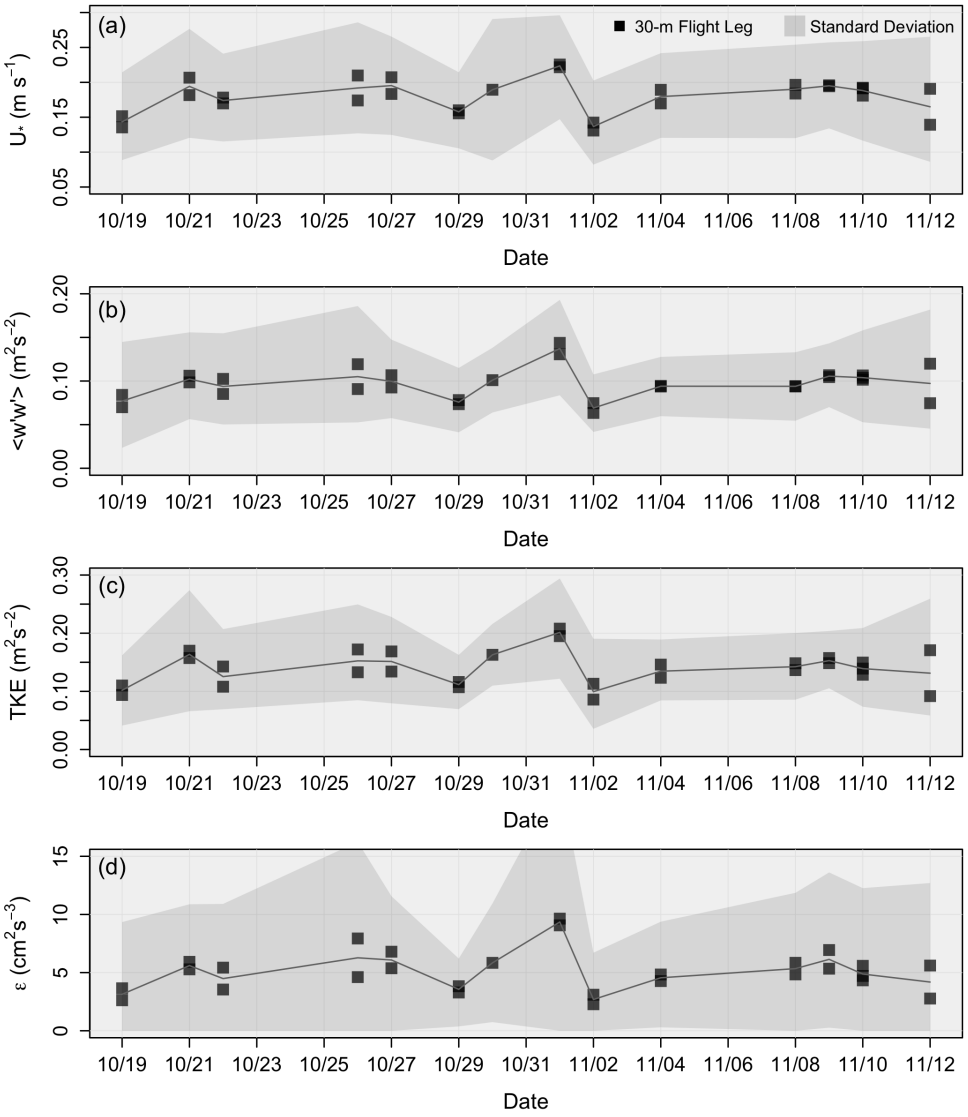

Figure 9. As in Figure 8, except for (a) Friction velocity (m^2s^{-2}); (b) Vertical velocity variance (m^2s^{-2}); (c) Turbulent kinetic energy (m^2s^{-2}); (d) Turbulent kinetic energy dissipation rate (cm^2s^{-3}).

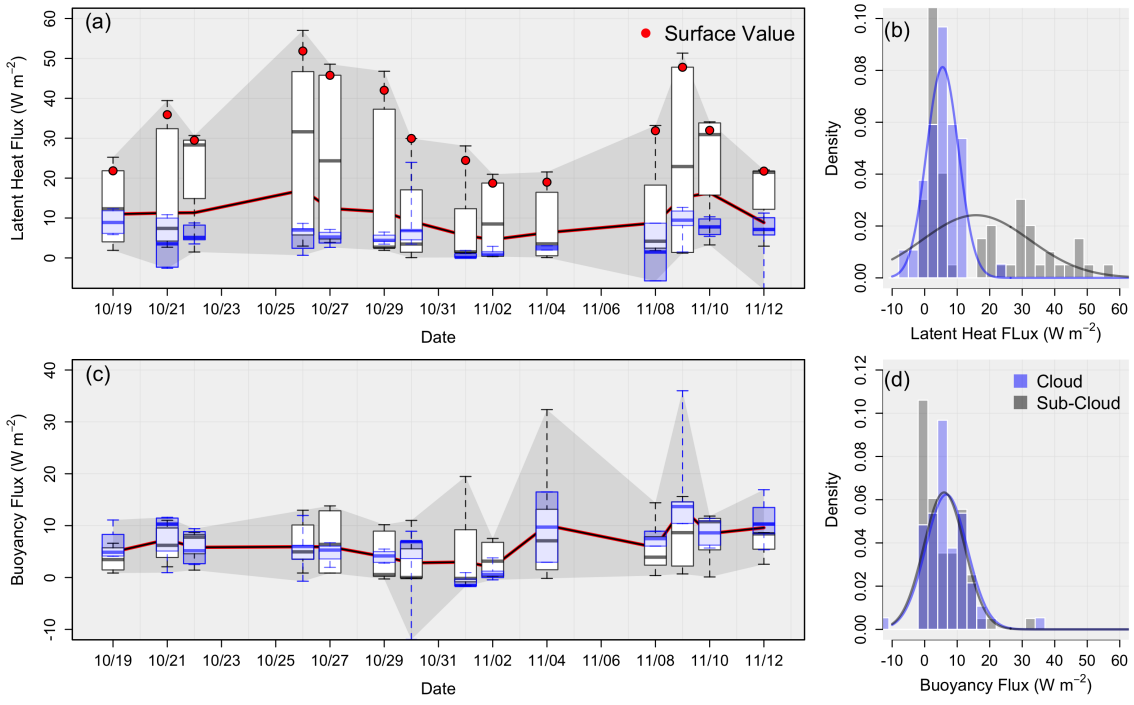

Figure 10. Boxplots of in-cloud (blue) and below cloud (white) data using mean values of horizontal flight legs for (a) the latent heat flux (Wm^{-2}) and (c) the Buoyancy flux (Wm^{-2}). Note that the gray envelope represents the range of the data, while the red line represents each flight mean values. Panels (b) and (d) shows the distributions of the data populations (with normal distributions overlaid for reference) for the latent heat flux and buoyancy flux, respectively.

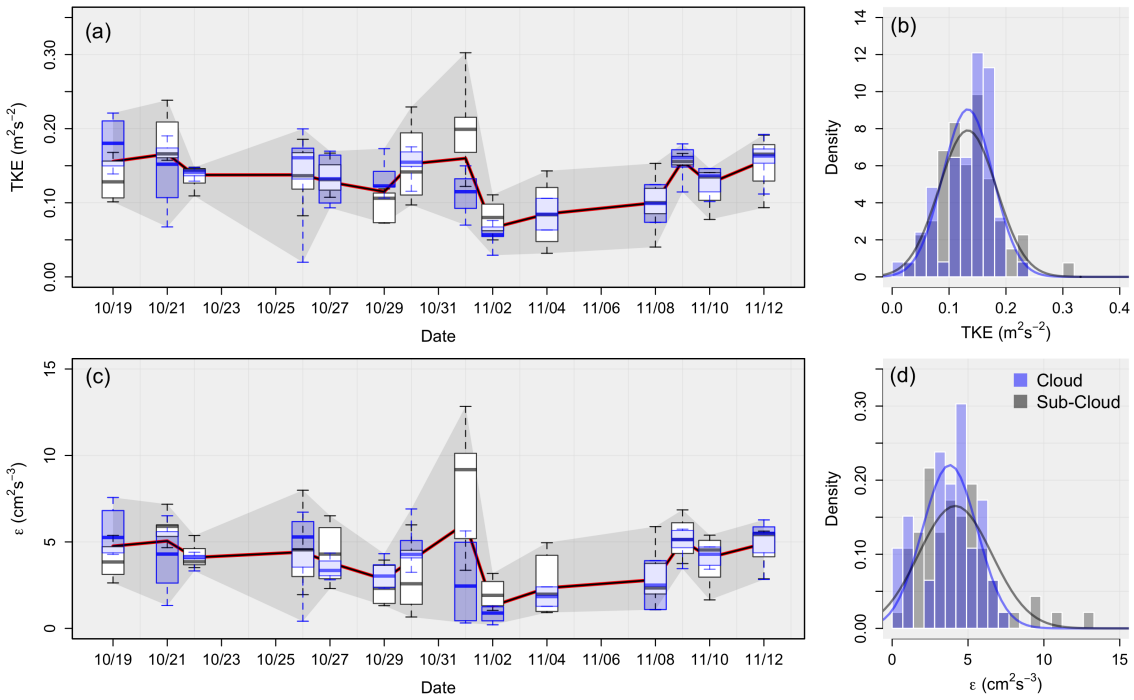

Figure 11. As in Figure 10, except for TKE ($m^2 s^{-2}$) in (a) and (b) and ϵ ($cm^{-2} s^{-3}$) in (c) and (d)

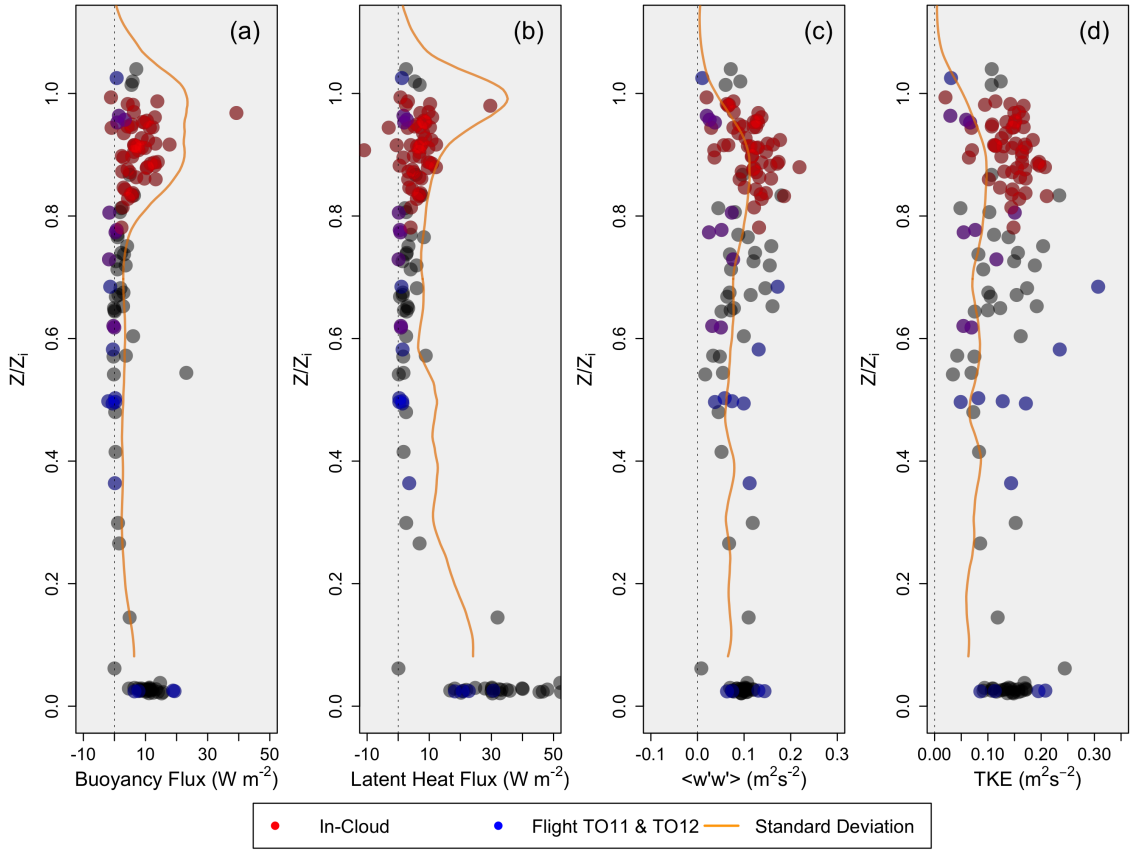

Figure 12. Mean values of horizontal flight legs plotted as a function of normalized boundary layer height. In-cloud data is red while data collected during Nov. 1^{st} and 2^{nd} is blue. The standard deviation is represented in orange. (a) Buoyancy flux (Wm^{-2}); (b) Latent heat flux (Wm^{-2}); (c) Vertical velocity variance ($\mathrm{m}^2\mathrm{s}^{-2}$); (d) TKE ($\mathrm{m}^2\mathrm{s}^{-2}$).

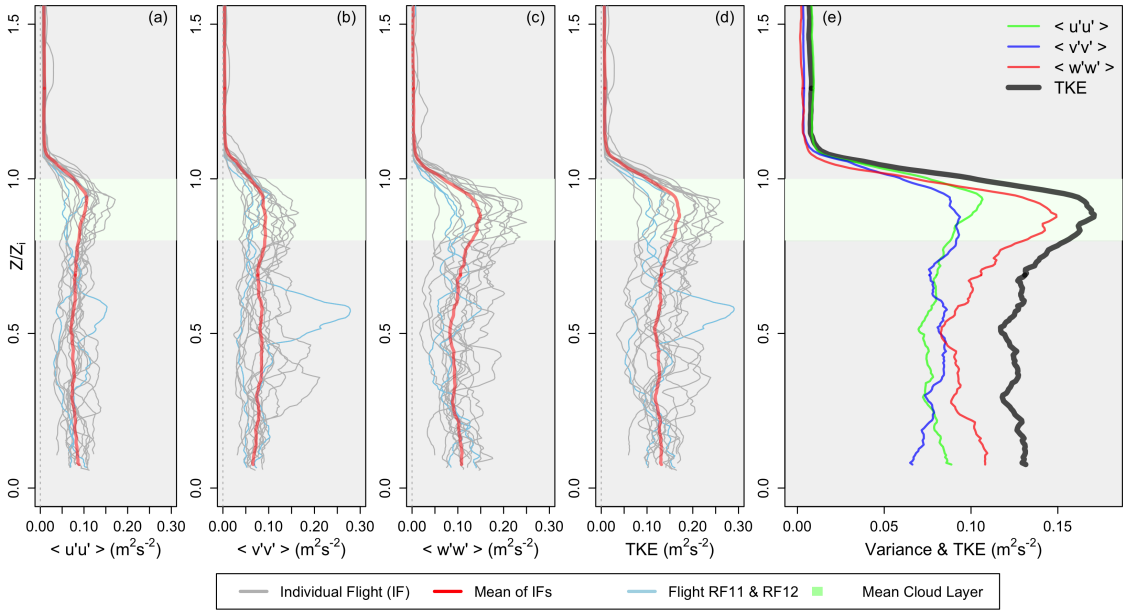

Figure 13. Vertical profiles (from data collected during flight profiles) of (a) u-variance (m^2s^{-2}); (b) v- variance (m^2s^{-2}); (c) w-variance (m^2s^{-2}); (d) TKE (m^2s^{-2}). Individual flights are displayed in gray, the mean value is displayed in red, with RF11 and RF12 shown in blue. Panel (e) shows the mean values from each of panels (a) through (d)

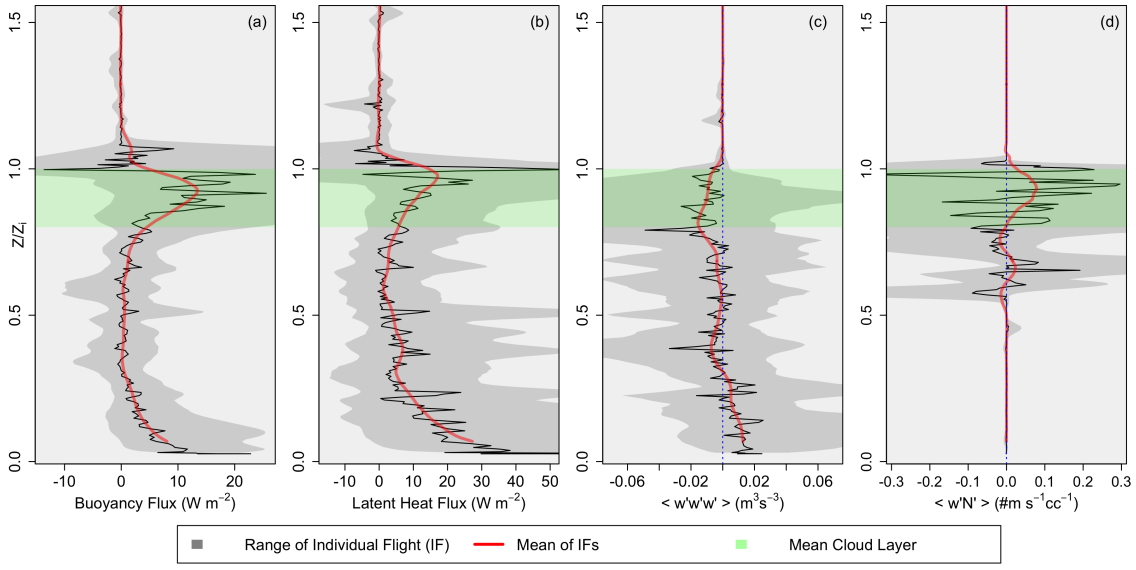

Figure 14. Vertical profiles (from data collected during flight profiles) of (a) Buoyancy flux ($\mathrm{Wm^{-2}}$); (b) Latent heat flux ($\mathrm{Wm^{-2}}$); (c) Vertical velocity skewness ($\mathrm{m^3s^{-3}}$); (d) cloud droplet flux ($\mathrm{ms^{-1}cc^{-1}}$). Note that the red line is the smoothed average of the raw data (black), while the gray envelope represents the range of values encountered.

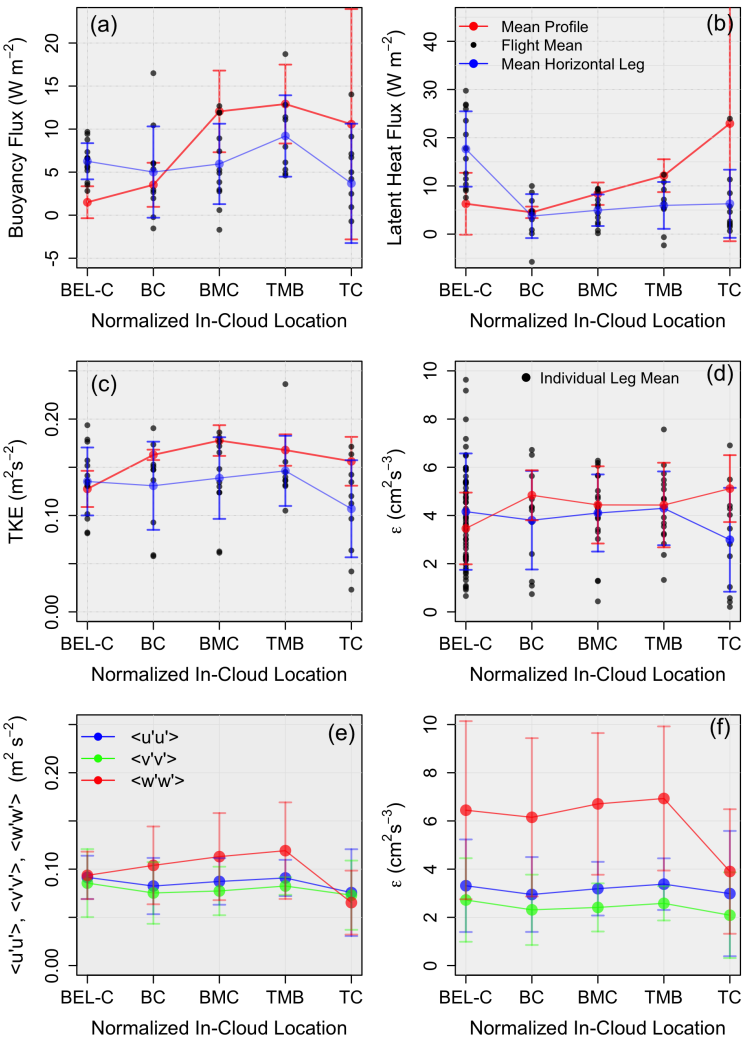

Figure 15. (a) Buoyancy flux (Wm^{-2}); (b) Latent heat flux (Wm^{-2}); (c) TKE ($\mathrm{m}^2\mathrm{s}^{-2}$); (d) TKE dissipation rate ($\mathrm{cm}^2\mathrm{s}^{-3}$). Data is divided into layers, including below-cloud (BEL-C), bottom of cloud (BC), bottom-middle of cloud (BMC), top-middle cloud (TMC), and top of cloud (TC). Red represents mean values for each layer using data collected during flight vertical profiles while blue represents mean values for each layer using data collected during horizontal flight legs. Black dots represent mean values for each flight using horizontal flight leg data. Note that the black dots in Panel (e) represent individual leg mean values as opposed to mean flight values. Panels (e) and (f) represent u (blue), v (green), and w (red) components of the TKE and TKE dissipation rate, respectively.

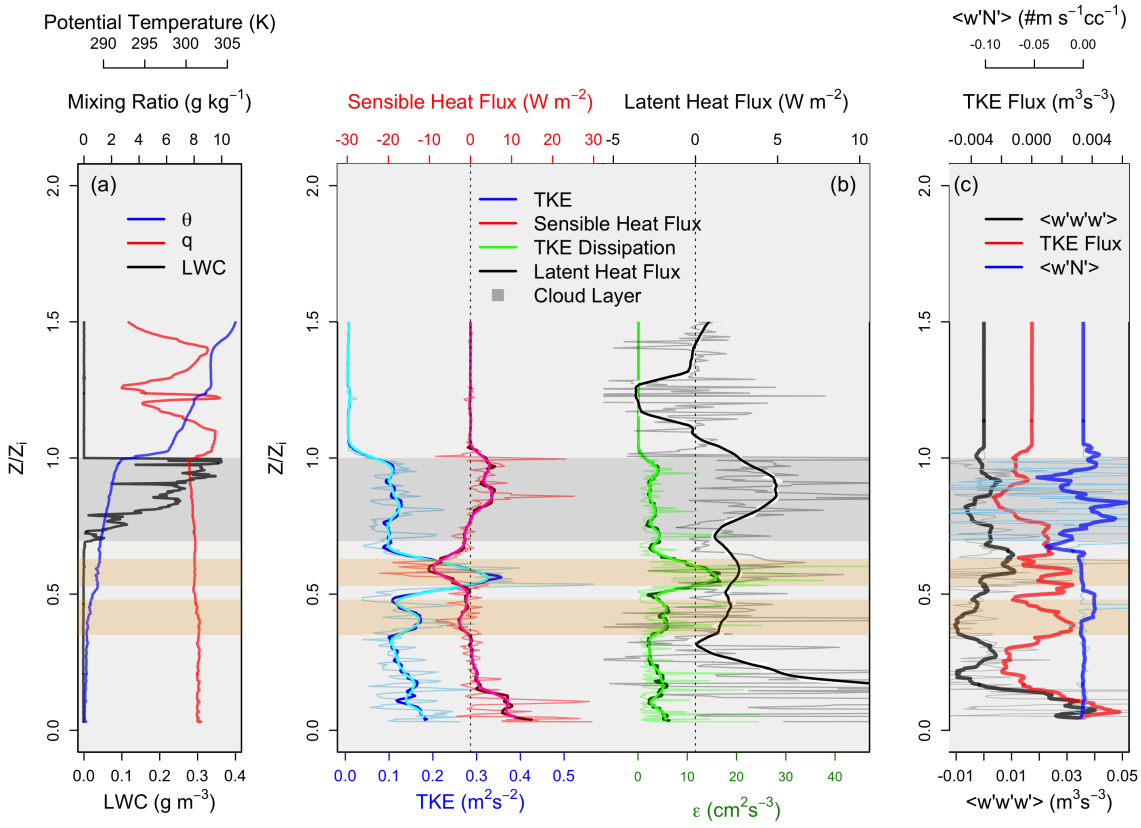

Figure 16. Vertical profiles as functions of normalized boundary layer height of (a) potential temperature (K) in blue, mixing ratio (g kg^{-1}) in red, and liquid water content (gm^{-3}) in black; (b) TKE (m^{2}s^{-2}) in blue, sensible heat flux (Wm^{-2}) in red, ϵ (cm^{2}s^{-3}) in green, and the latent heat flux (Wm^{-2}) in black. Note that the thin light colored lines represent raw values, while the dark thick lines represent smoothed averages; (c) $<w'w'w'>$ (m^{3}s^{-3}) in black, the TKE Flux (m^{3}s^{-3}) in red, and the droplet number concentration flux (m s^{-1}cc^{-1}) in blue. Note that the gray envelope represents the cloud layer, and the orange envelopes represent areas of interest (decoupling locations).

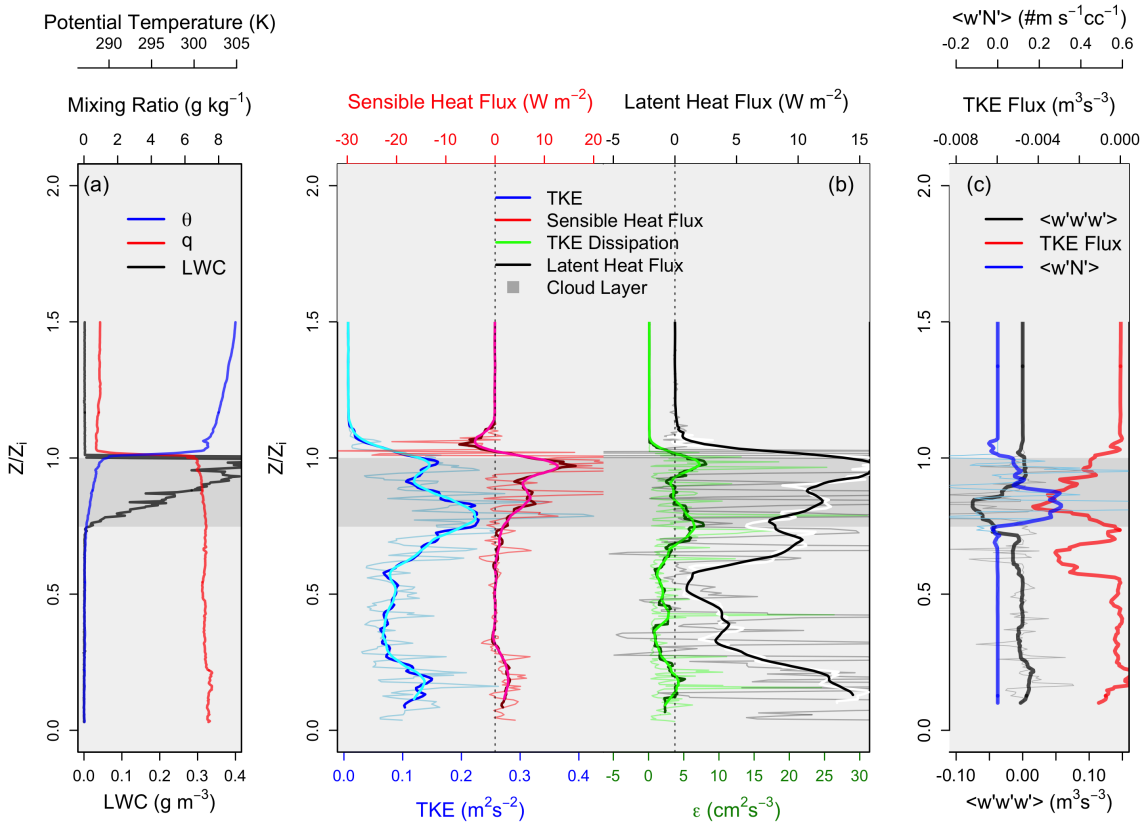

Figure 17. As in Figure 16, except for the well-mixed boundary layer case of RF03 (Oct 19^{th})

Table 1. Column (1): Research Flight (RF) identification; (2) The corresponding date; (3) Flight start and end times at Point Alpha. Note that local time: UTC – 4; (4) Boundary Layer conditions for each flight.

Flight	Date	Time (UTC)	BL Conditions
RF 3	Oct 19, 2008	12:05 - 14:40	Well Mixed
RF 4	Oct 21, 2008	12:10 - 14:50	Well Mixed
RF 5	Oct 22, 2008	12:00 - 14:40	Well Mixed
RF 7	Oct 26, 2008	12:00 - 15:00	Well Mixed
RF 8	Oct 27, 2008	15:55 - 19:00	Well Mixed
RF 9	Oct 29, 2008	11:50 - 15:00	Well Mixed
RF 10	Oct 30, 2008	11:50 - 15:00	Well Mixed
RF 11	Nov 01, 2008	12:05 - 15:05	Wind Shear / Moisture Above
RF 12	Nov 02, 2008	11:55 - 15:00	Moisture Above
RF 13	Nov 04, 2008	11:50 - 14:40	Wind Shear
RF 15	Nov 08, 2008	11:50 - 15:00	Decoupled
RF 16	Nov 09, 2008	11:50 - 15:05	Well Mixed
RF 17	Nov 10, 2008	14:45 - 18:00	Well Mixed
RF 18	Nov 12, 2008	11:50 - 15:15	Well Mixed

Table 2. Mean, standard deviation, and range of values for select variables over the 14 flights analyzed, with standard deviation values in parenthesis.

	Mean	**Range**
z_i (m)	1173 (119)	993 - 1450
Cloud Base (m)	936 (141)	716 - 1291
Cloud Thickness (m)	237 (101)	107 - 475
Boundary Layer θ (K)	289 (1.12)	287 - 291
Boundary Layer q (g kg^{-1})	7.51 (0.48)	6.83 - 8.32
$\Delta\theta$ (K)	16.8 (1.10)	13.89 - 18.42
Δq (g kg^{-1})	-5.53 (1.50)	-7.10 - 1.46
Boundary Layer PCASP (cc^{-1})	410 (127)	642 - 230
CDNC (cc^{-1})	262 (110)	80.5 - 423
Drop Size (μm)	12.33 (2.83)	9.6 - 20.5
Boundary Layer Wind Speed (m s^{-1})	4.42 (1.44)	2.03 - 6.31
Boundary Layer Wind Direction ($^\circ$)	170 (46)	NA
Free Atmosphere Wind Speed (m s^{-1})	5.16 (1.89)	2.83 - 8.34
Free Atmosphere Wind Direction ($^\circ$)	280 (115)	NA
α_θ	0.15 (0.08)	0.05 - 0.37
α_q	0.071 (0.049)	0.002 - 1.94
Δz_m (m)	363 (164)	108 - 653
Δz_b (m)	125 (136)	1.8 - 463

Table 3. Mean and range of values for select surface variables over the 14 flights analyzed, with standard deviation and the research flight number in parentheses for column mean and range, respectively.

	Mean	**Range**
Latent heat flux (Wm^{-2})	32.6 (11.5)	24.1 (RF 03) - 53.3 (RF 04)
Sensible heat flux (Wm^{-2})	8.6 (3.2)	3.93 (RF 03) - 17.1 (RF 01)
Bowen ratio	0.29 (0.15)	0.15 (RF 04) - 0.68 (RF 11)
Friction velocity (ms^{-1})	0.17 (0.023)	0.13 (RF 11) - 0.22 (RF12)
Vertical velocity variance (ms^{-1})	0.097 (0.017)	0.073 (RF 11) - 0.114 (RF 12)
TKE (m^{2}s^{-2})	0.14 (0.27)	0.051 (RF 11) - 0.20 (RF 12)
TKE dissipation rate (cm^{2}s^{-3})	5.14 (1.64)	9.40 (RF 11) - 2.64 (RF 12)

Table 4. Correlation coefficient values in the right-panel, with the variables in the left panel. Note that $\leftrightarrow$ divides the variables being compared. GPH is geopotential height and BLH is boundary layer height. N_a and N_D represent the aerosol number concentration and the cloud droplet number concentration, respectively.

	Correlation
BLH z_i $\leftrightarrow$ GPH	-0.37
ω $\leftrightarrow$ GPH	-0.89
Wind speed $\leftrightarrow$ GPH	0.14
Entrainment zone thickness $\leftrightarrow$ GPH	0.22
in-cloud ϵ $\leftrightarrow$ GPH	0.24
below cloud ϵ $\leftrightarrow$ GPH	-0.15
in-cloud TKE $\leftrightarrow$ GPH	0.23
below-cloud TKE $\leftrightarrow$ GPH	-0.19
in-cloud sensible heat flux $\leftrightarrow$ GPH	0.56
below-cloud sensible heat flux $\leftrightarrow$ GPH	0.49
in-cloud latent heat flux $\leftrightarrow$ GPH	0.29
below-cloud latent heat flux $\leftrightarrow$ GPH	0.22
SHF $\leftrightarrow$ wind speed	0.80
LHF $\leftrightarrow$ wind speed	0.36
z_i $\leftrightarrow$ wind speed	0.30
z_i $\leftrightarrow$ SHF	0.44
z_i $\leftrightarrow$ LHF	0.36
LHF $\leftrightarrow$ cloud thickness	-0.50
SHF $\leftrightarrow$ cloud thickness	-0.10
in-cloud ϵ $\leftrightarrow$ BLH	-0.34
belowsub-cloud ϵ $\leftrightarrow$ BLH	-0.13
in-cloud TKE $\leftrightarrow$ BLH	-0.32
belowsub-cloud TKE $\leftrightarrow$ BLH	-0.20
Sensible heat flux $\leftrightarrow$ BLH	0.36
Wind speed $\leftrightarrow$ sensible heat flux	0.64
Wind speed $\leftrightarrow$ BLH	0.30
N_a $\leftrightarrow$ TKE	0.35
N_D $\leftrightarrow$ TKE	0.42
drop size (μm) $\leftrightarrow$ TKE	-0.32
N_a $\leftrightarrow$ ϵ	0.37
N_D $\leftrightarrow$ ϵ	0.37
drop size (μm) $\leftrightarrow$ ϵ	-0.32

Table 5. Mean values for each layer discussed in Figure 15, where the top rows represent data calculated using flight vertical profiles, while the bottom rows represent data calculated using horizontal flight legs. See the text for exact partitioning of the cloud layer.

Vertical Profile Data	$<w'\theta_v'>$ (Wm^{-2})	$<w'q'>$ (Wm^{-2})	TKE ($\mathrm{m}^2\mathrm{s}^{-2}$)	ϵ ($\mathrm{cm}^2\mathrm{s}^{-3}$)
Below Cloud	1.95	7.83	0.129	3.43
Cloud Base	3.75	4.88	0.165	4.69
Bottom Middle	12.21	8.18	0.178	4.37
Top Middle	13.58	13.77	0.167	4.73
Cloud Top	10.57	21.05	0.154	5.03
Horizontal Leg Data				
Below Cloud	6.13	17.67	0.136	4.16
Cloud Base	4.55	4.50	0.131	3.81
Bottom Middle	6.10	5.03	0.139	4.10
Top Middle	8.30	7.56	0.145	4.30
Cloud Top	4.10	6.02	0.108	3.01